CZECH TECHNICAL UNIVERSITY IN PRAGUE

Faculty of Nuclear Sciences and Physical Engineering

Department of Physics

# Research project

## Measurement of coherent J/$\psi$ photoproduction in Pb-Pb collisions with ALICE

**Tomáš Herman**

**Supervisor: doc. Jesús Guillermo Contreras Nuño, Ph.D.**

**Prague, 2018**

ČESKÉ VYSOKÉ UČENÍ TECHNICKÉ
V PRAZE
Fakulta jaderná a fyzikálně inženýrská
Katedra fyziky

# Výzkumný úkol

## Měření koherentní $\mathrm{J}/\psi$ fotoprodukce v Pb-Pb srážkách na ALICE

**Tomáš Herman**

**Vedoucí práce: doc. Jesús Guillermo Contreras Nuño, Ph.D.**

**Praha, 2018**

ČESKÉ VYSOKÉ UČENÍ TECHNICKÉ V PRAZE
**FAKULTA JADERNÁ A FYZIKÁLNĚ INŽENÝRSKÁ**
PRAHA 1 - STARÉ MĚSTO, BŘEHOVÁ 7 - PSČ 115 19

**Katedra:** fyziky **Akademický rok:** 2017/2018

# VÝZKUMNÝ ÚKOL

***Student:*** Bc. Tomáš Herman

***Studijní program:*** Aplikace přírodních věd

***Obor:*** Experimentální jaderná a částicová fyzika

***Vedoucí úkolu:*** doc. Jesús Guillermo Contreras Nuño, Ph.D.

***Název úkolu (česky/anglicky):***
Měření koherentní J/ψ fotoprodukce v Pb-Pb srážkách na ALICE
Measurement of coherent J/ψ photoproduction in Pb-Pb collisions with ALICE

***Pokyny pro vypracování:***

1) Vypracovat rešerši na téma
   a. Měření koherentní J/ψ fotoprodukce v AA srážkách na PHENIX, CMS a ALICE.
   b. Modely koherentní J/ψ produkce v AA srážkách v rámci color-dipole modelu.
2) Měření koherentní J/ψ fotoprodukce v dopředné rapiditě v Pb-Pb srážkách z ALICE dat z LHC run 2

Výzkumný úkol bude vypracován v anglickém jazyce.
Součástí zadání výzkumného úkolu je jeho uložení na webové stránky katedry fyziky.

***Literatura:***

[1] Contreras, J.G. a Tapia Takaki, J.D. 2015. Ultra-peripheral heavy-ion collisions at the LHC. International Journal of Modern Physics A 30(8), s. 1542012
[2] Adam, J. et al. 2016. Measurement of an Excess in the Yield ofJ/ψat Very LowpTin Pb–Pb Collisions at sNN=2.76 TeV. Physical Review Letters 116(22)
[3] Khachatryan, V. et al. 2017. Coherent J/ ψ photoproduction in ultra-peripheral PbPb collisions at sNN = 2.76 TeV with the CMS experiment. Physics Letters B 772, s. 489–511
[4] Afanasiev, S. et al. 2009. Photoproduction of J /ψ and of high mass $e^+e^-$ in ultra-peripheral Au + Au collisions at sNN=200GeV. Physics Letters B 679(4), s. 321–329
[5] Lappi, T. a Mäntysaari, H. 2013. J/Ψ production in ultraperipheral Pb+Pb and p+Pb collisions at energies available at the CERN Large Hadron Collider. Physical Review C 87(3)
[6] Gonçalves, V.P. a Machado, M.V.T. 2011. Vector meson production in coherent hadronic interactions: Update on predictions for energies available at the BNL Relativistic Heavy Ion Collider and the CERN Large Hadron Collider. Physical Review C 84(1)

***Datum zadání:*** 27.10.2017

***Datum odevzdání:*** 30.06.2018

..........................................
*vedoucí katedry*

**Prohlášení:**

Prohlašuji, že jsem svůj Výzkumný úkol vypracoval samostatně a použil jsem pouze podklady ( literaturu, software, atd. ) uvedené v přiloženém seznamu.

Nemám závažný důvod proti použití tohoto školního díla ve smyslu § 60 Zákona č.121/2000 Sb., o právu autorském, o právech souvisejících s právem autorským a o změně některých zákonů (autorský zákon).

V Praze dne ............................. ........................

Tomáš Herman

# Acknowledgments

I would like to express my gratitude to my supervisor doc. Jesús Guillermo Contreras Nuño, Ph.D. for his guidance, for his patience, valuable advice and constructive comments, for his countless explanations and language corrections. I would also like to thank to Mgr. Michal Broz, Ph.D. for providing the analysed and Monte Carlo data sets.

*Title:*
**Measurement of coherent J/$\psi$ photoproduction in Pb-Pb collisions with ALICE**

*Author:* Tomáš Herman

*Specialization:* Experimental Physics and Particle Physics

*Sort of project:* Research project

*Supervisor:* doc. Jesús Guillermo Contreras Nuño, Ph.D., Department of Physics, Faculty of Nuclear Sciences and Physical Engineering, Czech Technical University in Prague

*Consultant:* ———

---

*Abstract:* Coherent J/$\psi$ photoproduction is a process in which a photon interacts with a target hadron and produces a J/$\psi$ meson. This can be achieved in Ultra-Peripheral Collisions (UPC). Ultra-peripheral collisions of lead ions at the LHC measured with the ALICE detector allow us to reach very low Bjorken $x$ and the measurement of coherent J/$\psi$ photoproduction cross section at such low Bjorken $x$ enables us to examine effects such as gluon saturation and shadowing. This Research project is dedicated to the analysis of coherent J/$\psi$ photoproduction in ultra-peripheral Pb-Pb collisions at centre-of-mass energies per nucleon $\sqrt{s_{NN}} = 5.02$ TeV measured with the ALICE detector in the forward rapidity region. The J/$\psi$ is reconstructed from its decay into two muons. Several articles concerning predictions for coherent J/$\psi$ photoproduction within the colour-dipole model as well as articles presenting the measurement of coherent J/$\psi$ photoproduction in ultra-peripheral, and for the first time peripheral, collisions are reviewed.

*Key words:* coherent photoproduction, J/$\psi$, ultra-peripheral collisions, colour-dipole model

*Název práce:*
**Měření koherentní $J/\psi$ fotoprodukce v Pb-Pb srážkách na ALICE**

*Autor:* Tomáš Herman

*Obor:* Experimentální jaderná a částicová fyzika

*Druh práce:* Výzkumný úkol

*Vedoucí práce:* doc. Jesús Guillermo Contreras Nuño, Ph.D., Katedra fyziky, Fakulta jaderná a fyzikálně inženýrská, České vysoké učení technické v Praze

*Konzultant:* ———

---

*Abstrakt:* Koherentní $J/\psi$ fotoprodukce je proces, ve kterém foton interaguje s hadronem a vyprodukuje $J/\psi$ mezon. Tohoto může být dosaženo v ultra-periferálních srážkách. Ultra-periferální srážky iontů olova na LHC měřené pomocí detektoru ALICE dovolují dosáhnout velmi nízkého Bjorkenova $x$ a měření účinného průřezu pro koherentní $J/\psi$ fotoprodukci při tak nízkém Bjorkenově $x$ dovoluje zkoumat efekty jako gluonová saturace a stínění. Tento Výzkumný úkol se věnuje analýze koherentní $J/\psi$ fotoprodukce v ultra-periferálních Pb-Pb srážkách, při těžišťové energii na nukleon $\sqrt{s_{NN}} = 5.02$ TeV, měřených pomocí detektoru ALICE v oblasti dopředné rapidity. Rekonstrukce $J/\psi$ probíhá z jeho rozpadu na dva miony. Několik článků zabývajících se předpověďmi pro koherentní $J/\psi$ fotoprodukci v rámci barevného dipólového modelu a měřením koherentní $J/\psi$ fotoprodukce v ultra-periferálních, a poprvé také v periferálních, srážkách je také popsáno.

*Klíčová slova:* koherentní fotoprodukce, $J/\psi$, ultra-periferální srážky, barevný dipólový model

# Contents

# List of Figures

# List of Tables

# Preface

Coherent $J/\psi$ photoproduction is a process in which a photon interacts with a target hadron (either a proton or a nucleus) and produces a $J/\psi$ meson. This can be achieved in Ultra-Peripheral Collisions (UPC), where two ions or an ion and a proton collide with large enough impact parameter, so that they do not interact strongly, but still can interact electromagnetically.

Ultra-peripheral collisions of lead ions at the LHC measured with the ALICE detector allow us to reach very low Bjorken $x$ and the measurement of coherent $J/\psi$ photoproduction cross section at such low Bjorken $x$ enables us to examine effects such as gluon saturation and shadowing.

A brief review of two articles on theoretical predictions for coherent $J/\psi$ photoproduction cross section in ultra-peripheral collisions within the colour-dipole model is presented in Chapter 1.

In Chapter 2 are reviewed two articles concerning the measurement of the coherent $J/\psi$ photoproduction cross section in ultra-peripheral collisions by PHENIX at RHIC and CMS at LHC. The third paper, by the ALICE collaboration, is the first paper to report a measurement of coherent $J/\psi$ photoproduction cross section in peripheral collisions.

Chapter 3 is dedicated to the analysis of coherent $J/\psi$ photoproduction in ultra-peripheral Pb-Pb collisions at centre-of-mass energy per nucleon $\sqrt{s_{NN}} = 5.02$ TeV measured with the ALICE detector in the forward rapidity region. The $J/\psi$ is reconstructed from its decay into two muons. The main focus of this chapter is the extraction of the coherent contribution to the overall $J/\psi$ signal from the transverse momentum spectrum.

# Chapter 1

# Models of coherent J/$\psi$ photoproduction in AA collisions within the colour-dipole model

Predictions for coherent J/$\psi$ photoproduction cross section in AA collisions within the colour-dipole model from two papers are reviewed in this chapter. First, the predictions by T. Lappi and H. Mäntysaari [1] are presented. Then the the predictions by V.P. Gonçalves and M.V.T. Machado [2] are presented. A basic introduction into the theory of Ultra-Peripheral Collisions (UPC) can be found in [3] and for an overview look into [4].

## 1.1 J/$\psi$ production in ultra-peripheral Pb+Pb and p+Pb collisions at energies available at the CERN Large Hadron Collider

"J/$\psi$ production in ultra-peripheral Pb+Pb and p+Pb collisions at energies available at the CERN Large Hadron Collider" [1] is a paper by T. Lappi and H. Mäntysaari.

In the dipole picture the virtual photon emitted by the lead nucleus fluctuates into a quark-antiquark colour dipole which then can strongly interact with the target. The dipole model is valid only for small Bjorken $x$, thus an $x < 0.02$ condition is required for the target parton. The dipole-proton cross section can be parametrised like

$$\frac{\mathrm{d}\sigma^{\mathrm{p}}_{\mathrm{dip}}}{\mathrm{d}^2\mathbf{b}_T}(\mathbf{b}_T, \mathbf{r}_T, x_{\mathbb{P}}) = 2\mathcal{N}(\mathbf{r}_T, \mathbf{b}_T, x_{\mathbb{P}}), \tag{1.1}$$

where $\mathbf{b}_T$ is the impact parameter of the $\gamma$-p collision, $\mathbf{r}_T$ is the transverse size of the dipole, $x_{\mathbb{P}}$ is the Bjorken variable of Deep-Inelastic Scattering (DIS) in a diffractive event and $\mathcal{N}$ is the imaginary part of the forward dipole-proton scattering amplitude.

The dipole-proton amplitude $\mathcal{N}$ satisfies the Balitsky-Kovchegov (BK) evolution equation. The best approach would be to fit the initial conditions of the BK evolution equation to the available data from DIS, solve the BK equation and use the computed dipole amplitude.

For this calculation it is necessary to know the impact parameter dependence of the amplitude. However, when the impact parameter dependence is added to the BK equation, it leads to a non-physical growth of the size of the proton. Therefore, two phenomenological dipole cross section parametrisations, including realistic impact parameter dependence, were used.

First one is the IIM [5] dipole cross section which includes the most important features of the BK evolution. The values of the parameters for the cross section are taken from a fit to HERA data [6]. The second model is a factorised approximation of the IPsat model with eikonalised DGLAP (Dokshitzer–Gribov–Lipatov–Altarelli–Parisi) evolved gluon distribution [7, 8].

In the IIM model the impact parameter dependence is factorised as

$$\frac{\mathrm{d}\sigma^{\mathrm{p}}_{\mathrm{dip}}}{\mathrm{d}^2\mathbf{b}_T}(\mathbf{b}_T,\mathbf{r}_T,x) = 2T_p(\mathbf{b}_T)\mathcal{N}(\mathbf{r}_T,x), \tag{1.2}$$

Based on [9], the impact parameter profile function is chosen as

$$T_p(\mathbf{b}_T) = \exp\left(-b^2/2B_p\right), \tag{1.3}$$

where $B_p = 5.59\ \mathrm{GeV}^{-2}$.

In the IPsat model the impact parameter dependence is included in the saturation scale as

$$\frac{\mathrm{d}\sigma^{\mathrm{p}}_{\mathrm{dip}}}{\mathrm{d}^2\mathbf{b}_T}(\mathbf{b}_T,\mathbf{r}_T,x) = 2\left[1-\exp\left(-r^2F(x,r)T_p(\mathbf{b}_T)\right)\right], \tag{1.4}$$

where $r = |\mathbf{r}_T|$ and $T_p(\mathbf{b}_T)$ is defined same as in Eq. 1.3, but with $B_p = 4.0\ \mathrm{GeV}^{-2}$. $F(x,r)$ is proportional to the DGLAP evolved gluon distribution and is equal to

$$F(x,r) = \frac{1}{2\pi B_p}\frac{\pi^2}{2N_{\mathrm{c}}}\alpha_{\mathrm{s}}\left(\mu_0^2+\frac{C}{r^2}\right)xg\left(x,\mu_0^2+\frac{C}{r^2}\right), \tag{1.5}$$

where $N_C$ is the number of colours, $C = 4$ and $\mu_0^2 = 1.17\ \mathrm{GeV}^2$ [8]. Following [10] Eq. 1.4 is replaced by a factorised approximation

$$\frac{\mathrm{d}\sigma^{\mathrm{p}}_{\mathrm{dip}}}{\mathrm{d}^2\mathbf{b}_T}(\mathbf{b}_T,\mathbf{r}_T,x) \approx 2T_p(\mathbf{b}_T)\left[1-\exp\left(-r^2F(x,r)\right)\right], \tag{1.6}$$

where $T_p(\mathbf{b}_T)$ and $F(x,r)$ stay the same. This approximation transforms the IPsat parametrisation to the form of Eq. 1.2 with $\mathcal{N}(r,x) = \left[1-\exp\left(-r^2 F(x,r)\right)\right]$ and it is denoted as fIPsat.

The quasi-elastic (coherent and incoherent) vector meson production cross section in nuclear DIS is

$$\frac{\mathrm{d}\sigma^{\gamma^* A \to VA}}{\mathrm{d}t} = \frac{R_g^2(1+\beta^2)}{16\pi} \left\langle |\mathcal{A}(x_{\mathbb{P}}, Q^2, \Delta_T)|^2 \right\rangle_{\mathrm{N}}, \tag{1.7}$$

where $-Q^2$ is the virtuality of the photon, $\Delta_T$ is the transferred momentum, $1+\beta^2$ accounts for the real part of the amplitude and the $R_g$ is a correction for the skewedness effect (gluons in the target having slightly different $x$). The prescription for these factors is taken from [11]

$$\beta = \tan\frac{\pi\lambda}{2}, \tag{1.8}$$

$$R_g = \frac{2^{2\lambda+3}}{\sqrt{\pi}} \frac{\Gamma(\lambda+5/2)}{\Gamma(\lambda+4)}, \tag{1.9}$$

where

$$\lambda = \frac{\partial \ln \mathcal{A}}{\partial \ln 1/x_{\mathbb{P}}}. \tag{1.10}$$

The correction terms are important in the absolute normalisation of the cross section and are necessary to describe HERA data.

For the coherent cross section the amplitude $\mathcal{A}$ is squared after averaging ,$|\langle \mathcal{A} \rangle_{\mathrm{N}}|^2$, and for the incoherent cross section the variance is used $\left\langle |\mathcal{A}|^2 \right\rangle_{\mathrm{N}} - |\langle \mathcal{A} \rangle_{\mathrm{N}}|^2$. To compute the average values the following formula is used [12]

$$\langle \mathcal{O}(\{\mathbf{b}_{Ti}\}) \rangle_{\mathrm{N}} \equiv \int \prod_{i=1}^{A} \left[\mathrm{d}^2\mathbf{b}_{Ti} T_A(\mathbf{b}_{Ti})\right] \mathcal{O}(\{\mathbf{b}_{Ti}\}). \tag{1.11}$$

It is the average over the position of the nucleon in the nucleus. $T_A$ is the Woods-Saxon distribution with nuclear radius $R_A = (1.12A^{1/3} - 0.86A^{-1/3})$ fm and surface thickness $d = 0.54$ fm.

The imaginary part of the scattering amplitude $\mathcal{A}$ is the Fourier transform of the dipole-target cross section $\sigma_{\mathrm{dip}}$ from impact parameter $\mathbf{b}_T$ to momentum transfer $\Delta_T$, contracted with the overlap between the vector meson and the virtual photon wave function.

$$\mathcal{A}(x_{\mathbb{P}}, Q^2, \Delta_T) = \int \mathrm{d}^2\mathbf{r}_T \int \frac{\mathrm{d}z}{4\pi} \int \mathrm{d}^2\mathbf{b}_T [\Psi_V^* \Psi](r, Q^2, z) e^{-i\mathbf{b}_T \cdot \Delta_T} \frac{\mathrm{d}\sigma_{\mathrm{dip}}}{\mathrm{d}^2\mathbf{b}_T}(\mathbf{b}_T, \mathbf{r}_T, x_{\mathbb{P}}). \tag{1.12}$$

The Boosted Gaussian and the Gauss-LC parametrisations [8] are used to describe the overlap of the wave functions of the photon splitting into the quark-antiquark pair and of this pair forming the vector meson.

For a large and smooth nucleus the averaged amplitude is

$$\left\langle \mathcal{A}(x_{\mathbb{P}}, Q^2, \Delta_T) \right\rangle_{\mathrm{N}} = \int \frac{\mathrm{d}z}{4\pi} \mathrm{d}^2\mathbf{r}_T \, \mathrm{d}^2\mathbf{b}_T e^{-i\mathbf{b}_T \cdot \Delta_T} [\Psi_V^* \Psi](r, Q^2, z) \\ \times 2 \left[1 - \exp\left\{-2\pi B_p A T_A(b) \mathcal{N}(r, x_{\mathbb{P}})\right\}\right]. \quad (1.13)$$

At large transferred momentum $-t = \Delta_T{}^2$ the cross section is strongly dominated by the incoherent contribution. Therefore the incoherent cross section at large $|t|$ is the total quasi-elastic cross section which can be computed as the average value of the squared amplitude $\left\langle |\mathcal{A}|^2 \right\rangle_{\mathrm{N}}$. This approach results in [10]

$$\left\langle \left|\mathcal{A}_{q\bar{q}}\right|^2 (x_{\mathbb{P}}, Q^2, \Delta_T) \right\rangle_N = 16\pi B_p A \int \mathrm{d}^2\mathbf{b}_T \int \mathrm{d}^2\mathbf{r}_T \, \mathrm{d}^2\mathbf{r}_T{}' \frac{\mathrm{d}z}{4\pi} \frac{\mathrm{d}z'}{4\pi} [\Psi_V^* \Psi](r, Q^2, z) \\ \times [\Psi_V^* \Psi](r', Q^2, z') e^{-B_p \Delta_T{}^2} e^{-2\pi B_p A T_A(b)[\mathcal{N}(r) + \mathcal{N}(r')]} \left( \frac{\pi B_p \mathcal{N}(r) \mathcal{N}(r') T_A(b)}{1 - 2\pi B_p T_A(b) \left[\mathcal{N}(r) + \mathcal{N}(r')\right]} \right). \quad (1.14)$$

Following [13] the vector meson production cross section in nucleus-nucleus (or proton-nucleus) collisions is factorised as the product of the photon flux generated by one of the nuclei and the photon-nucleus cross section

$$\sigma^{pA \to \mathrm{J}/\psi A} = \int \mathrm{d}\omega \frac{n(\omega)}{\omega} \sigma^{\gamma A \to \mathrm{J}/\psi A}(\omega), \quad (1.15)$$

where $\sigma^{\gamma A \to \mathrm{J}/\psi A}$ is the photon-nucleus cross section, $n(\omega)$ is the photon flux, $\omega = (M_V/2)e^y$ is the energy of the photon, $M_V$ is the vector meson mass and $y$ is the vector meson rapidity.

In nucleus-nucleus collision both of the nuclei can act as the photon source, therefore

$$\frac{\mathrm{d}\sigma^{A_1 A_2 \to \mathrm{J}/\psi A_1 A_2}}{\mathrm{d}y} = n^{A_2}(y) \sigma^{\gamma A_1}(y) + n^{A_1}(-y) \sigma^{\gamma A_2}(-y). \quad (1.16)$$

In proton-nucleus collision the proton can also act as the photon source, but as the generated photon flux is proportional to the square of the electric charge of the emitting particle, the case when the photon is emitted from the nucleus dominates.

The Bjorken $x$ of the probed gluon, denoted $x_{\mathbb{P}}$, is

$$x_{\mathbb{P}} = M_V e^{-y}/\sqrt{s_{\rm NN}}. \tag{1.17}$$

For forward and backward rapidity this means either a small energy photon scattering off a large-$x$ gluon or a large energy photon scattering off a small-$x$ gluon. At mid rapidity only a moderately small-$x$ gluons are probed. The presented predictions should be most reliable in this region.

A comparison of the predictions of coherent J/$\psi$ photoproduction cross section with the ALICE data [14, 15] can be seen in Fig. 1.1.

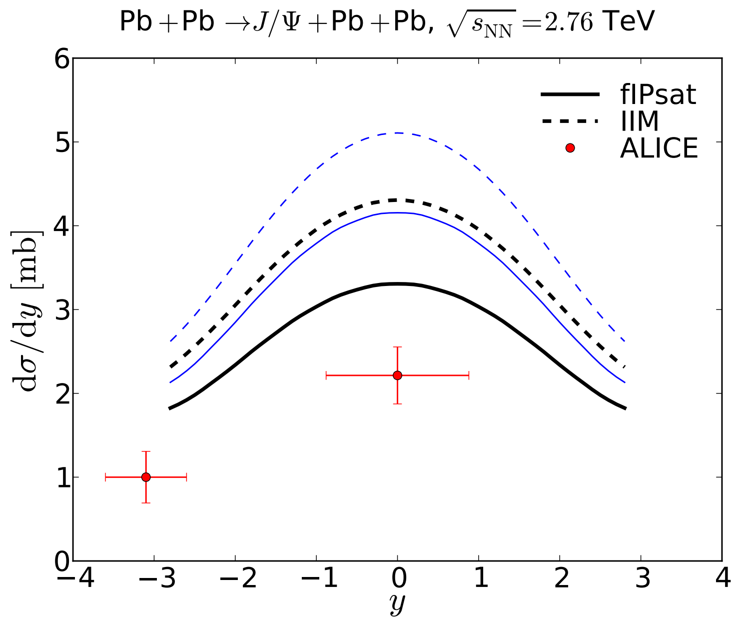


Figure 1.1: The coherent J/$\psi$ photoproduction cross section prediction for Pb+Pb collisions at $\sqrt{s_{\rm NN}} = 2.76$ TeV computed with the fIPsat and IIM parametrisations and the Boosted Gaussian (thin blue lines) and Gauss-LC (thick black lines) wave functions compared with the ALICE data ([14, 15]) [1].

The ALICE data seems to favour the fIPsat model over the IIM model. With regard to this, the most important difference between the models is the impact parameter dependence. The IIM parametrisation uses $B_p = 5.59$ GeV$^{-2}$, which comes from a fit to inclusive J/$\psi$ production and the IIM model is close to the value measured for the inclusive J/$\psi$ production. The IPsat parametrisation has smaller $B_p = 4.0$ GeV$^{-2}$, which comes from a fit to exclusive J/$\psi$ production measured by HERA, therefore the fIPsat model is considered more reliable for the exclusive J/$\psi$ photoproduction.

The ALICE data also seems to favour the Gauss-LC wave function over the Boosted Gaussian, therefore the fIPsat model with the Gauss-LC wave function is considered to be the most reliable combination.

The PHENIX collaboration has measured the coherent J/$\psi$ photoproduction cross section in Au+Au collisions at $\sqrt{s_{NN}}$ = 200 GeV to be $\left.\frac{d\sigma_{J/\psi+Xn}}{dy}\right|_{|y|<0.35} = 76 \pm 31\,(\text{stat}) \pm 15\,(\text{syst})\ \mu\text{b}$ [16]. And the fIPsat dipole cross section parametrisation with the Gauss-LC wave function predicts 109 $\mu$b.

The presented results are slightly higher than the measured values, but the rapidity dependence is reproduced correctly. The fIPsat model with the Gauss-LC wave function is consistently above all data points by a factor of approximately 1.4. Note that all the parametrisations used are older than the ALICE data. They describe well the HERA data, but no nuclear data were used to constrain them. The normalisation error is most likely caused by the skewedness correction. The corrections is larger for ALICE data than for HERA data, making it less reliable.

The prediction for the incoherent J/$\psi$ photoproduction cross section can be seen in Fig. 1.2.

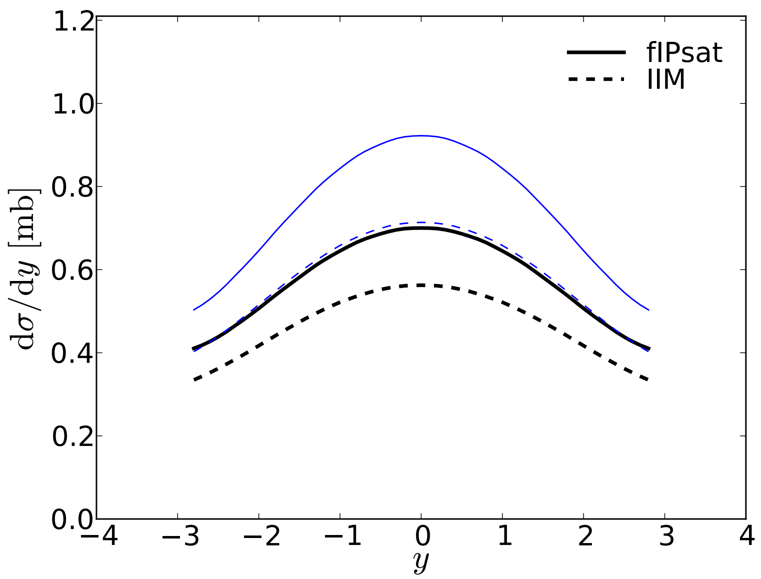


Figure 1.2: The incoherent J/$\psi$ photoproduction cross section prediction for Pb+Pb collisions at $\sqrt{s_{\text{NN}}} = 2.76$ TeV computed with the fIPsat and IIM parametrisations and the Boosted Gaussian (thin blue lines) and Gauss-LC (thick black lines) wave functions [1].

The normalisation of the different models varies quite a lot again, but the rapidity dependence remains very similar. Now the normalisation is larger for the fIPsat model, this is due to different impact parameter parametrisation, see [10].

In Fig. 1.3 is presented the prediction for the $t$ distribution of the J/$\psi$ photoproduction at mid rapidity ($x_{\mathbb{P}} \approx 0.001$).

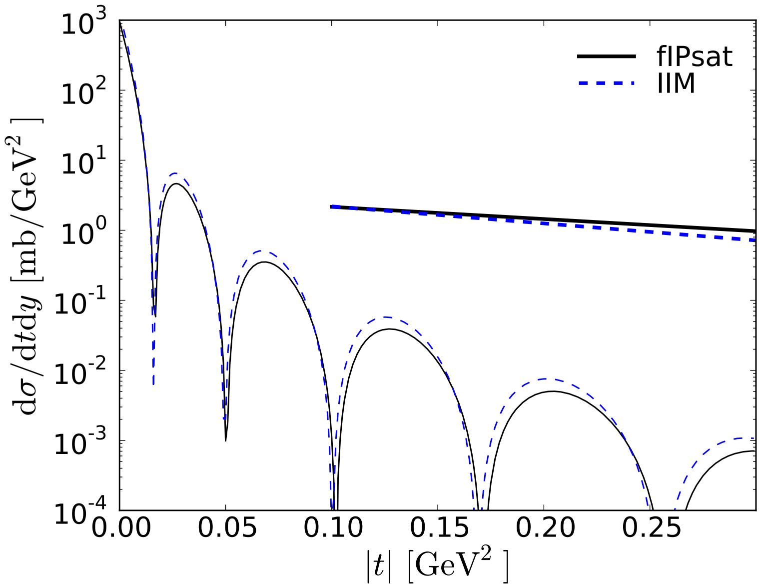


Figure 1.3: The coherent (thick lines) and incoherent (thin lines) J/$\psi$ photoproduction cross section in lead-lead collision at $\sqrt{s_{\mathrm{NN}}} = 2.76$ TeV as a function of momentum transfer $t$ at midrapidity $y = 0$ using the Gaus-LC wave function [1].

The $t$ distribution for incoherent J/$\psi$ production cross section directly measures the spatial distribution of partons (gluons) in the nucleon.

In Fig. 1.4 is presented the prediction for the rapidity dependence of the J/$\psi$ photoproduction cross section in proton-lead collisions (the photon-nucleus scattering is required to be coherent). The difference between the model's normalisation is reduced, because the dominant process is now the photon-proton scattering, which is constrained by HERA data.

In Fig. 1.5 the incoherent J/$\psi$ photoproduction cross section in lead-lead collision is divided by $\mathrm{A_{Pb}}$ times the coherent J/$\psi$ photoproduction cross section in proton-lead collision, both at $\sqrt{s_{\mathrm{NN}}} = 2.76$. Because in proton-lead ultra-peripheral collisions the main process is a photon-proton collision, the above mentioned ratio is the nuclear transparency ratio, which measures the absorption of the colour dipole as it propagates through the nucleus.

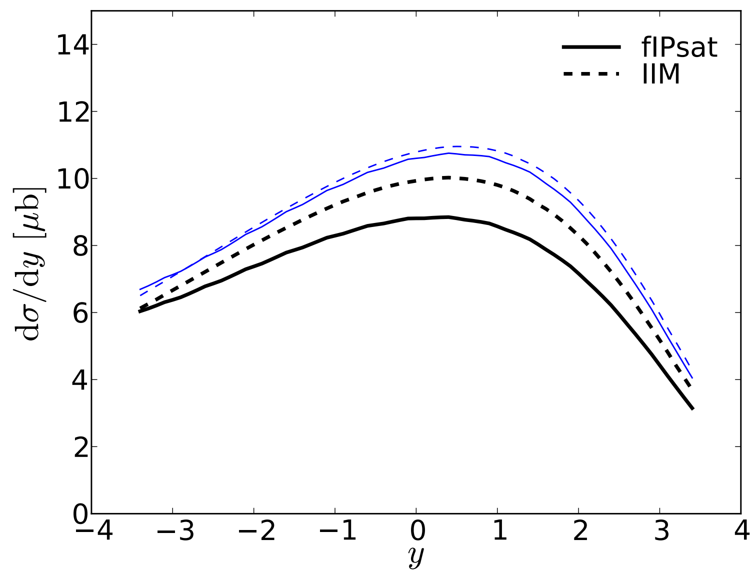


Figure 1.4: The J/$\psi$ photoproduction cross section in proton-lead collisions at $\sqrt{s_{\rm NN}} = 5.02$ TeV computed using the fIPsat and IIM parametrisations and the Boosted Gaussian (thin blue lines) and Gauss-LC (thick black lines) wave functions. The proton is moving in the negative $y$ direction [1].

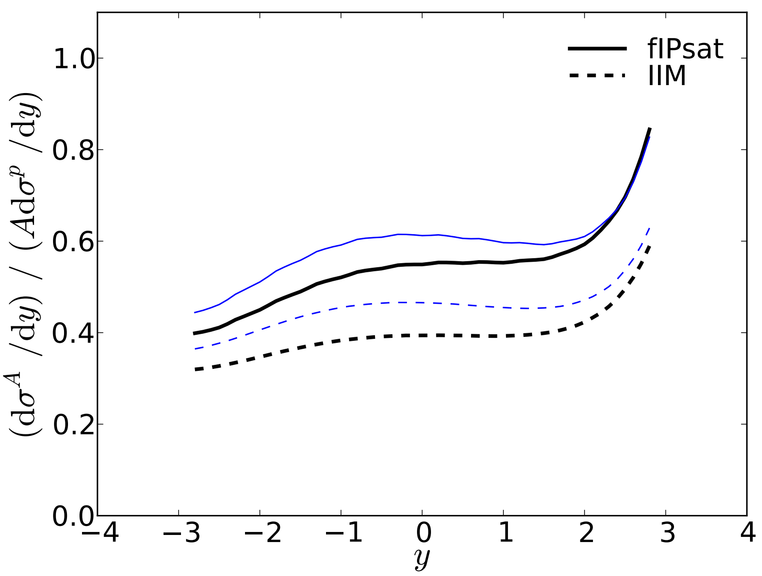


Figure 1.5: The nuclear transparency ratio at $\sqrt{s_{\rm NN}} = 2.76$ TeV computed using the fIPsat and IIM parametrisations and the Boosted Gaussian (thin blue lines) and Gauss-LC (thick black lines) wave functions. The proton is moving in the negative $y$ direction [1].

## 1.2 Vector Meson Production in Coherent Hadronic Interactions: An update on predictions for RHIC and LHC

”Vector Meson Production in Coherent Hadronic Interactions: An update on predictions for RHIC and LHC” [2] is a paper by V.P. Gonçalves and M.V.T. Machado.

The coherent vector meson ($V$) photoproduction cross section in a hadron-hadron collision is given by

$$\sigma(hh \to Vh) = 2 \int_{\omega_{min}}^{\infty} \mathrm{d}\omega \int \mathrm{d}t \, \frac{\mathrm{d}N_\gamma(\omega)}{\mathrm{d}\omega} \frac{\mathrm{d}\sigma}{\mathrm{d}t} \left(W_{\gamma h}, t\right) , \tag{1.18}$$

where $\frac{\mathrm{d}N_\gamma(\omega)}{\mathrm{d}\omega}$ is the equivalent photon flux, $\frac{\mathrm{d}\sigma}{\mathrm{d}t}\left(W_{\gamma h}, t\right)$ is the differential cross section for the process $(\gamma h \to Vh)$, $\omega$ is the photon energy, $\omega_{min} = M_V^2/4\gamma_L m_p$ is the minimum photon energy with $M_V$ being the vector meson mass, $\gamma_L$ is the Lorentz boost of a single beam, $m_p$ is the mass of a proton, $W_{\gamma h}^2 = 2\,\omega\sqrt{s_{\mathrm{NN}}}$ is the c.m.s energy of the photon-hadron system with $\sqrt{s_{\mathrm{NN}}}$ is the c.m.s energy of the hadron-hadron system and $t = -\Delta^2$, where $\Delta$ is the transferred transverse momentum.

For ultra-peripheral collisions the equivalent photon flux of a nuclei can be approximated as [17, 13, 18]

$$\frac{\mathrm{d}N_\gamma(\omega)}{\mathrm{d}\omega} = \frac{2Z^2\alpha_{em}}{\pi\,\omega} \left[\bar{\eta}\, K_0(\bar{\eta}) K_1(\bar{\eta}) + \frac{\bar{\eta}^2}{2}\mathcal{U}(\bar{\eta})\right] , \tag{1.19}$$

where $Z$ is the charge of the hadron, $\alpha_{em}$ is the fine-structure constant, $K_0(\bar{\eta})$ and $K_1(\bar{\eta})$ are the modified Bessel functions, $\bar{\eta} = \omega\,(2R_h)/\gamma_L$ with $R_h$ being the hadron radius and $\mathcal{U}(\bar{\eta}) = K_1^2(\bar{\eta}) - K_0^2(\bar{\eta})$. The factor 2 in Eq. 1.19 takes into account that both nuclei can act as the either the source or the target.

For proton-proton collisions the photon flux is given by [19]

$$\frac{\mathrm{d}N_\gamma(\omega)}{\mathrm{d}\omega} = \frac{\alpha_{\mathrm{em}}}{2\pi\,\omega}\left[1 + \left(1 - \frac{2\,\omega}{\sqrt{s_{NN}}}\right)^2\right]\left(\ln\Omega - \frac{11}{6} + \frac{3}{\Omega} - \frac{3}{2\Omega^2} + \frac{1}{3\,\Omega^3}\right), \tag{1.20}$$

where $\Omega = 1 + [(0.71\,\mathrm{GeV}^2)/Q^2_{\mathrm{min}}]$ and $Q^2_{\mathrm{min}} = \omega^2/[\gamma_L^2\,(1 - 2\,\omega/\sqrt{s_{NN}})] \approx (\omega/\gamma_L)^2$.

Within the colour dipole approach, the vector meson (V) production amplitude is calculated as [20, 21, 8]

$$\mathcal{A}_{T,L}^{\gamma^* h \to Vh}(x, Q^2, \Delta) = \int \mathrm{d}z\, \mathrm{d}^2\mathbf{r}\, (\Psi^{V*}\Psi)_{T,L}\, \mathcal{A}_{q\bar{q}}(x, \mathbf{r}, \Delta)\,, \tag{1.21}$$

where $x$ is the Bjorken variable, $Q^2$ is the photon virtuality, $z\,(1-z)$ is the longitudinal momentum fraction of the quark (antiquark), $\mathbf{r}$ is the transverse size of the dipole, $(\Psi^{V*}\Psi)_{T,L}$ is the photon-vector meson wave function overlap and $\mathcal{A}_{q\bar{q}}$ is the dipole-target elastic scattering amplitude, which is connected to the scattering amplitude $\mathcal{N}(x, \mathbf{r}, \mathbf{b})$ by [8]

$$\mathcal{A}_{q\bar{q}}(x, \mathbf{r}, \Delta) \;=\; i \int \mathrm{d}^2\mathbf{b}\, e^{-i\mathbf{b}.\Delta}\, 2\mathcal{N}(x, \mathbf{r}, \mathbf{b})\,, \tag{1.22}$$

where $\mathbf{b}$ is the impact parameter. With Eq. 1.22 the amplitude for the exclusive vector meson photoproduction can be expressed as

$$\mathcal{A}_{T,L}^{\gamma^* h \to Vh}(x, Q^2, \Delta) \;=\; i \int \mathrm{d}z\, \mathrm{d}^2\mathbf{r}\, \mathrm{d}^2\mathbf{b} e^{-i[\mathbf{b}-(1-z)\mathbf{r}]\Delta} (\Psi_V^*\Psi)_T\, 2\mathcal{N}(x, \mathbf{r}, \mathbf{b}), \tag{1.23}$$

where the $[i(1-z)\mathbf{r}]\Delta$ factor arises from non-forward corrections to the wave functions [22]. The differential cross section for exclusive vector meson photoproduction is given by

$$\frac{\mathrm{d}\sigma_{T,L}}{\mathrm{d}t}(\gamma^* h \to Vh) = \frac{1}{16\pi} |\mathcal{A}_{T,L}^{\gamma^* p \to Vh}(x, Q^2, \Delta)|^2\, (1+\beta^2)\,, \tag{1.24}$$

where $\beta$ is the ratio of the real to imaginary part of the scattering amplitude. The skewedness corrections are also taken into account, for details see [21, 8].

The scattering amplitude $\mathcal{N}(x, \mathbf{r}, \mathbf{b})$ contains all information about the target and the strong interaction physics. For the photon-nucleus collision the scattering amplitude can be assumed to be given by [23]

$$\mathcal{N}(x, \mathbf{r}, \mathbf{b}) = \left\{ 1 - \exp\left[ -\frac{1}{2} A T_A(\mathbf{b})\, \sigma_{dip}(x, \mathbf{r}) \right] \right\}\,, \tag{1.25}$$

where $T_A(\mathbf{b})$ is the nuclear profile function and $\sigma_{dip}(x, \mathbf{r})$ is the IIM [5] parametrisation of the dipole-nucleon cross section.

For the photon-proton collision the scattering amplitude can be described by the MPS [24] non-forward saturation model, which describes well the dependence on energy, photon virtuality and momentum transfer in HERA data. The dipole-target elastic scattering amplitude in the MPS model is given by

$$\mathcal{A}_{q\bar{q}}(x,r,\Delta) = \sigma_0\, e^{-B|t|}\mathcal{N}\left(rQ_{\rm sat}(x,|t|),x\right), \tag{1.26}$$

where $\sigma_0$ is the normalisation parameter, the $B$ parameter has value $B = 3.754$ GeV$^{-2}$ [24] and

$$Q^2_{\rm sat}\left(x,|t|\right) = Q_0^2(1+c|t|)\left(\frac{1}{x}\right)^{\lambda}. \tag{1.27}$$

The rapidity distribution of the coherent vector meson photoproduction can be computed as

$$\frac{\mathrm{d}\sigma\ [h+h\to h\otimes V\otimes h]}{\mathrm{d}y} = \omega\frac{\mathrm{d}N_\gamma(\omega)}{\mathrm{d}\omega}\,\sigma_{\gamma h\to V\,h}\left(\omega\right), \tag{1.28}$$

where $\otimes$ represents a rapidity gap.

The prediction for the rapidity distribution of J/$\psi$ and $\Upsilon$ photoproduction cross section in p+p collisions at $\sqrt{s} = 7$ TeV at the LHC is presented in Fig. 1.6.

At central rapidity the photoproduction cross section is $\frac{d\sigma}{dy}(y=0)\simeq 6.5$ nb (18 pb) for $J/\Psi$ ($\Upsilon$). In Tab. 1.1 are presented predictions for the integrated photoproduction cross sections (production rates) assuming a luminosity $\mathscr{L}^{\rm pp}_{\rm LHC} = 10^7$ mb$^{-1}$s$^{-1}$.

The prediction for the rapidity distribution of the $\rho$ and J/$\psi$ photoproduction cross sections in Au+Au collisions at $\sqrt{s} = 200$ GeV at RHIC is presented in Fig. 1.7. In Tab. 1.1 are presented predictions for the integrated photoproduction cross sections (production rates) assuming a luminosity $\mathscr{L}^{\rm AuAu}_{\rm RHIC} = 0.4$ mb$^{-1}$s$^{-1}$.

In Fig. 1.8 is presented the prediction for the rapidity dependence of the ratio between the J/$\psi$ and $\rho$ photoproduction cross sections. The presented prediction is without the correction for mutual nuclear excitation, which is rapidity dependent and for the integrated cross section gives an overall suppression factor of 1/10 [25]. The presented ratio J/$\psi$/$\rho$ should have small sensitivity to the correction and at mid rapidity $\frac{d\sigma(\rho^0)}{dy}/\frac{d\sigma(J/\Psi)}{dy}\simeq 1.2\times 10^3$.

The prediction for the rapidity distribution of $\rho$ and J/$\psi$ photoproduction cross section in Pb+Pb collisions at $\sqrt{s_{NN}} = 2.76$ TeV at the LHC is presented in Fig. 1.9.

At central rapidity the photoproduction cross section is $\frac{d\sigma}{dy}(y=0)\simeq 3.8$ mb (470 mb) for J/$\psi$ ($\rho$). And in Tab. 1.1 are presented predictions for the integrated photoproduction cross sections (production rates) assuming a luminosity $\mathscr{L}^{\rm PbPb}_{\rm LHC} = 0.42$ mb$^{-1}$s$^{-1}$.

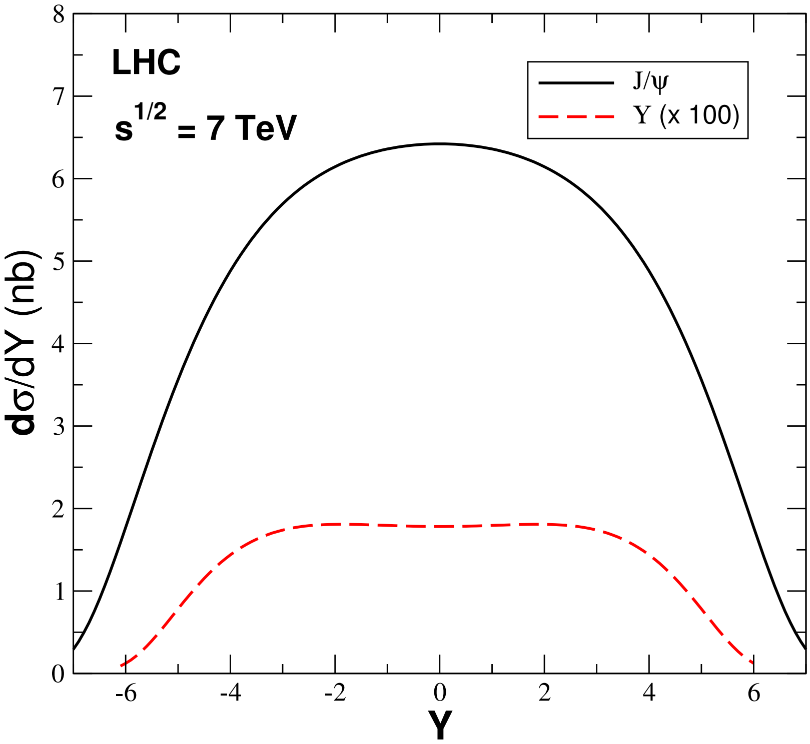


Figure 1.6: Prediction for the rapidity distribution of J/$\psi$ and $\Upsilon$ photoproduction cross section in p+p collisions at $\sqrt{s} = 7$ TeV at the LHC [2].

| Meson | **RHIC (Au+Au)** | **LHC (Pb+Pb)** | **LHC (p+p)** |
|---|---|---|---|
| $\rho$ | 609.7 mb (256.0) | 4276 mb (1796.0) | — |
| J/$\psi$ | 0.51 mb (0.20) | 20 mb (8.40) | 63.70 nb (637.0) |
| $\Upsilon$ | — | — | 0.18 nb (1.80) |

Table 1.1: The integrated cross section (events rate/second) for vector meson photoproduction in p+p and A+A collisions at RHIC and LHC energies [2].

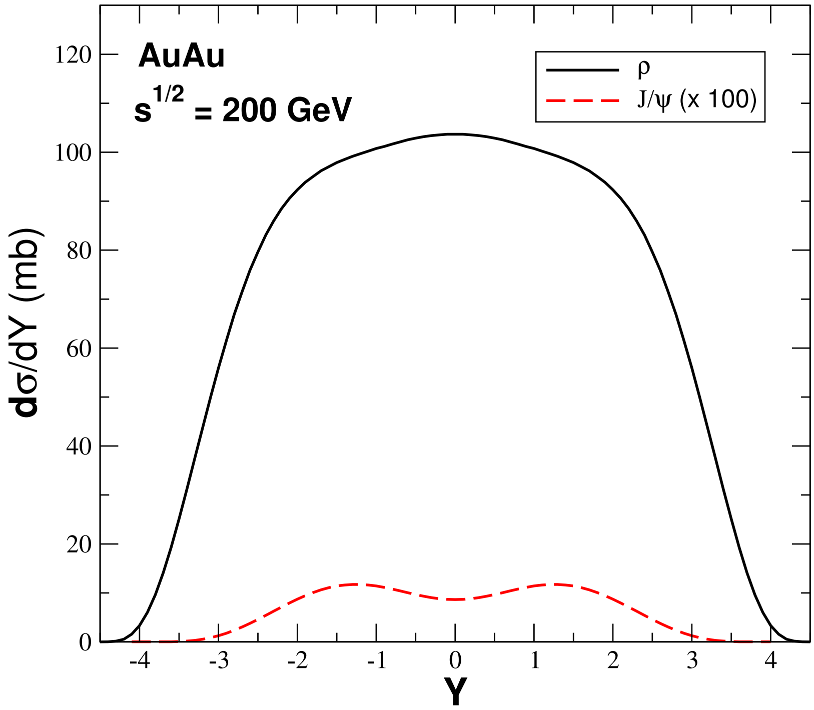


Figure 1.7: Prediction for the rapidity distribution of $\rho$ and $J/\psi$ photoproduction cross section in Au+Au collisions at $\sqrt{s} = 200$ GeV at the RHIC [2].

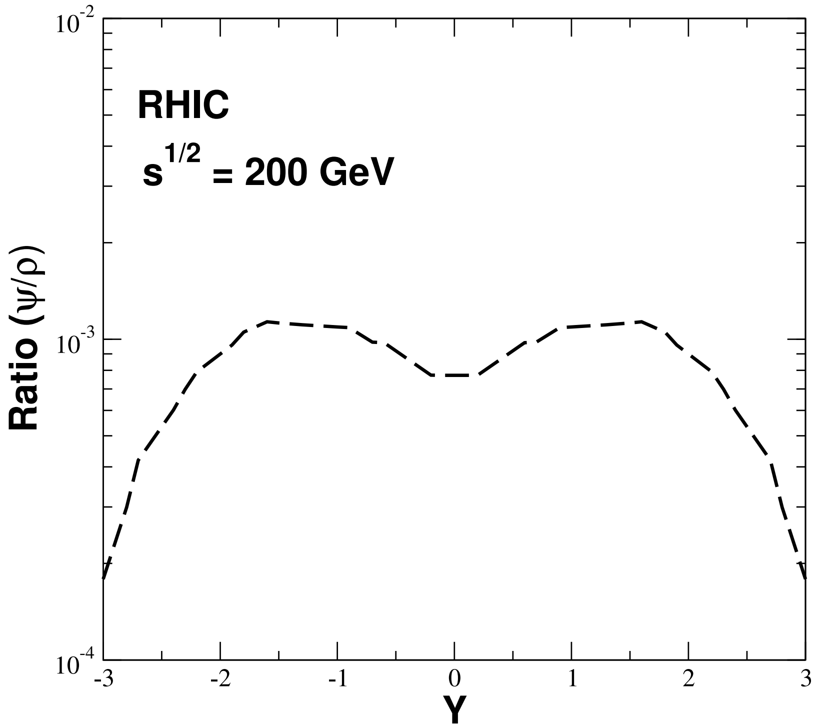


Figure 1.8: Prediction for the rapidity dependence of the ratio between the $J/\psi$ and $\rho$ photoproduction cross sections [2].

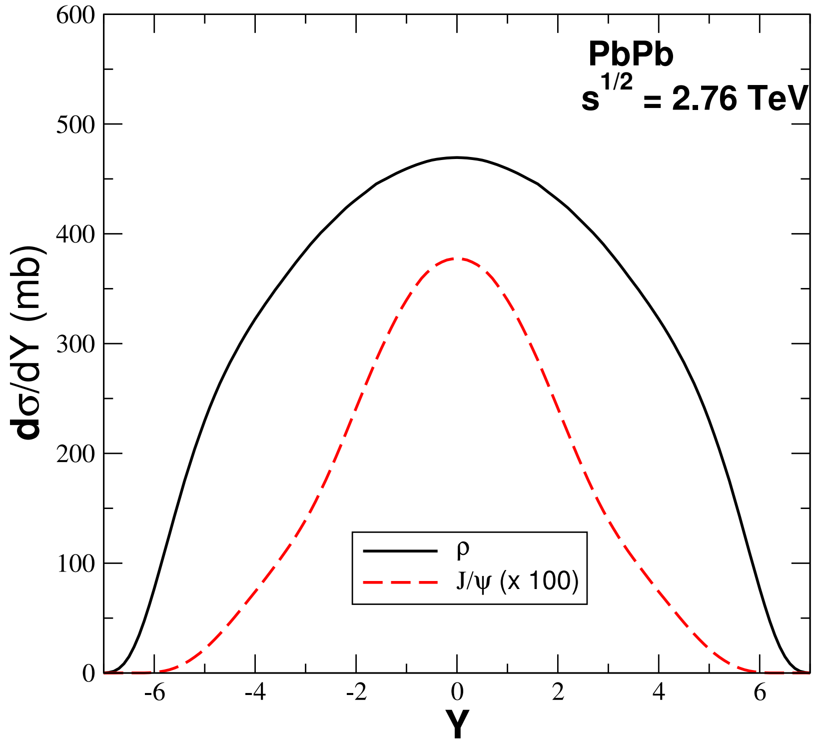


Figure 1.9: Prediction for the rapidity distribution of $\rho$ and J/$\psi$ photoproduction cross section in Pb+Pb collisions at $\sqrt{s_{NN}} = 2.76$ TeV at the LHC [2].

# Chapter 2

# Previous measurements of coherent J/$\psi$ photoproduction in AA collisions

Results of several papers focusing on coherent J/$\psi$ photoproduction in AA collisions are reviewed in this chapter. To begin with, the PHENIX paper presenting first results of J/$\psi$ photoproduction in ultra-peripheral collisions, using Au+Au data at $\sqrt{s_{NN}}$ = 200 GeV [16], is discussed. Next, the coherent J/$\psi$ photoproduction in ultra-peripheral PbPb collisions at $\sqrt{s_{NN}}$ = 2.76 TeV with the CMS experiment [26] is presented. At last, the ALICE paper reporting the first measurement of an excess in the yield of J/$\psi$ at very low $p_T$ in Pb–Pb collisions at $\sqrt{s_{NN}}$ = 2.76 TeV [27] is reviewed.

## 2.1 Photoproduction of J/$\psi$ and of high mass $e^+e^-$ in ultra-peripheral Au+Au collisions at $\sqrt{s_{\mathrm{NN}}}$ = 200 GeV

"Photoproduction of J/$\psi$ and of high mass $e^+e^-$ in ultra-peripheral Au+Au collisions at $\sqrt{s_{\mathrm{NN}}} = 200$ GeV" [16] is a paper by the PHENIX Collaboration, where are presented the first results of heavy vector meson (J/$\psi$) production in UPC.

The analysed data were collected by the PHENIX detector at RHIC during the high-luminosity Au+Au run in 2004. The data were selected by the UPC trigger:

1. Veto on coincident signals in both Beam-Beam Counters (BBC) to select exclusive-type events, i.e. with a large rapidity gap on either side of the central arm.

2. EMCal-Trigger (ERT) with a 2×2 tile threshold at 0.8 GeV. The efficiency for triggering at least one of the $e^\pm$ is estimated to be $\varepsilon = 0.9 \pm 0.1$.

3. Minimum of 30 GeV of energy deposited in one or both of the Zero Degree Calorimeters (ZDCs), in order to select events with forward neutron emission.

The forward neutron emission is due to Coulomb excitation by the electromagnetic fields of the accelerated ions. The probability of the Coulomb excitation can be factorised, therefore it does not introduce any bias in the measurement, and it is 55% $\pm$ 6% for the coherent $J/\psi$ photoproduction. For the incoherent $J/\psi$ photoproduction probability of forward neutron emission is $\approx$ 100%, but in this case it is due to nucleus break-up.

The complete trigger efficiency is estimated to be $\varepsilon = 0.9 \pm 0.1$ from the second trigger condition, as the contributions from the first and third conditions were calculated to be negligible.

The total number of events collected by the trigger was 8.5 millions, but only 6.7 millions satisfied standard data quality assurance criteria. The event sample corresponded to an integrated luminosity of $\mathscr{L}_{int} = 141 \pm 12\ \mu\mathrm{b}^{-1}$, computed from the minimum-bias trigger events.

To enhance the amount of gamma-induced events the following global cuts were also applied:

1. Standard off-line vertex cut $|vtx_z| < 30$ cm to select collisions well centred in the detector.

   Normally the vertex position is obtained via timing information from BBC and/or ZDC, but this does not work for UPC. By definition there are no coincidences in the BBC and often there are also no coincidences in the ZDC. Therefore, for this analysis the vertex position was reconstructed via the position of hits in the multi-wire proportional chamber (PC) and of clusters in the electromagnetic calorimeter (EMCal).

2. Only events with two charged particles. This criteria is used in order to select exclusive processes characterised by only two isolated charged particles in the final state.

   It allows them to suppress non-UPC (mainly beam-gas and peripheral collisions) reactions that also passed the UPC trigger, while loosing less then 5% of the signal.

Unlike in previous $J/\psi$ measurements in Au+Au nuclear collisions, which have to deal with large particle multiplicities, in UPC the detector environment is rather clean and no strict electron identification cuts are needed. Instead, the following offline cuts were used:

1. Ring-Imaging Cherenkov detector (RICH) multiplicity $n_0 \geq 2$ selects $e\pm$ which fire two or more tubes around the track within the ring radius.

2. Candidate tracks associated with an EMCal cluster with dead or noisy towers within a 2$\times$2 tile are excluded.

3. At least one of the two electron/positron tracks is required to have energy higher then 1 GeV, because of the behaviour of the ERT (discussed above), which has a 0.8 GeV threshold with turn-on curve.

In order to identify coherent events a cut selecting only candidate $e^+e^-$ detected in opposite arms of the detector was used. But after all the previous selections this cut affected only one event.

Acceptance and efficiency corrections were obtained from the PHENIX GEANT3 simulation with input from the STARLIGHT Monte Carlo.

The J/$\psi$ were reconstructed by an invariant mass fit of the measured $e^+e^-$ pairs. The invariant mass spectrum and fit can be seen in Fig. 2.1. After the analysis cuts no remaining like-sign background was observed. The shape of the spectrum is consistent with the two expected processes: the photoproduction of the $e^+e^-$ continuum (exponential) and the J/$\psi \to e^+e^-$ decay (Gaussian).

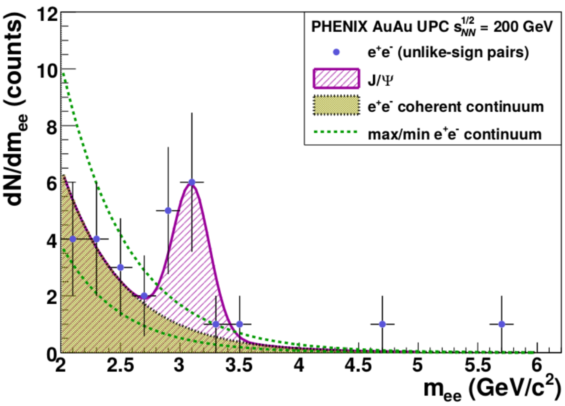


(a)

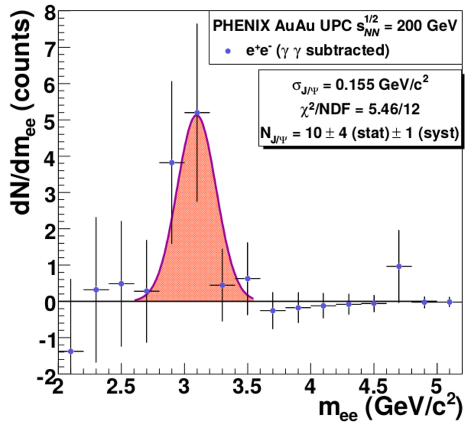


(b)

Figure 2.1: (a) Invariant mass distribution of $e^+e^-$ pairs with the fit of a dielectron continuum (exponential distribution) and a J/$\psi$ (Gaussian) signal. The two additional dashed curves indicate the fit results with the maximum and minimum continuum contributions considered. (b) J/$\psi$ invariant mass distribution after subtracting the fitted dielectron continuum signal [16].

The data is fitted with three free parameters: the exponential normalisation, the J/$\psi$ peak normalisation and width (the position has been fixed at the known J/$\psi$ mass). The width is consistent with the J/$\psi$ width from MC.

Systematic uncertainties of the fit were obtained by changing the exponential shape of the fit to a power law fit and by varying the slope parameter by $\pm 3\sigma$. The total number of J/$\psi$ is calculated to be $N_{J/\psi}$ = 9.9 ± 4.1 (stat) ± 1.0 (syst) and the number of $e^+e^-$ pairs in the background continuum is $N_{e^+e^-}$ = 13.7 ± 3.7 (stat) ± 1.0 (syst) for a mass range $m_{e^+e^-} \in$ [2.0,2.8] GeV/c$^2$

In Fig. 2.2 is shown an invariant mass vs. $p_T$ scatter plot. It can be seen that most of the events outside the J/$\psi$ peak have very low transverse momenta ($p_T \lesssim 100$ MeV/$c$), which is expected for the coherent background. Near the J/$\psi$ mass peak there are also higher $p_T$ events. Coherent J/$\psi$ production can only yield events with $p_T \lesssim 200$ MeV/$c$, on the other hand incoherent J/$\psi$ production can yield events with much higher $p_T$. The contribution of both processes is expected to be of the same order.

If the incoherent sample is assumed to correspond to events in the J/$\psi$ mass window with $p_T^2 > 0.1$ (0.05) GeV$^2$/c$^2$, it corresponds to approximately 4 (6) counts. This is about 40 (60)% of the total J/$\psi$ events, which is compatible with the theoretical prediction. Limited data statistics does not allow to obtain a better separation of the two contributions

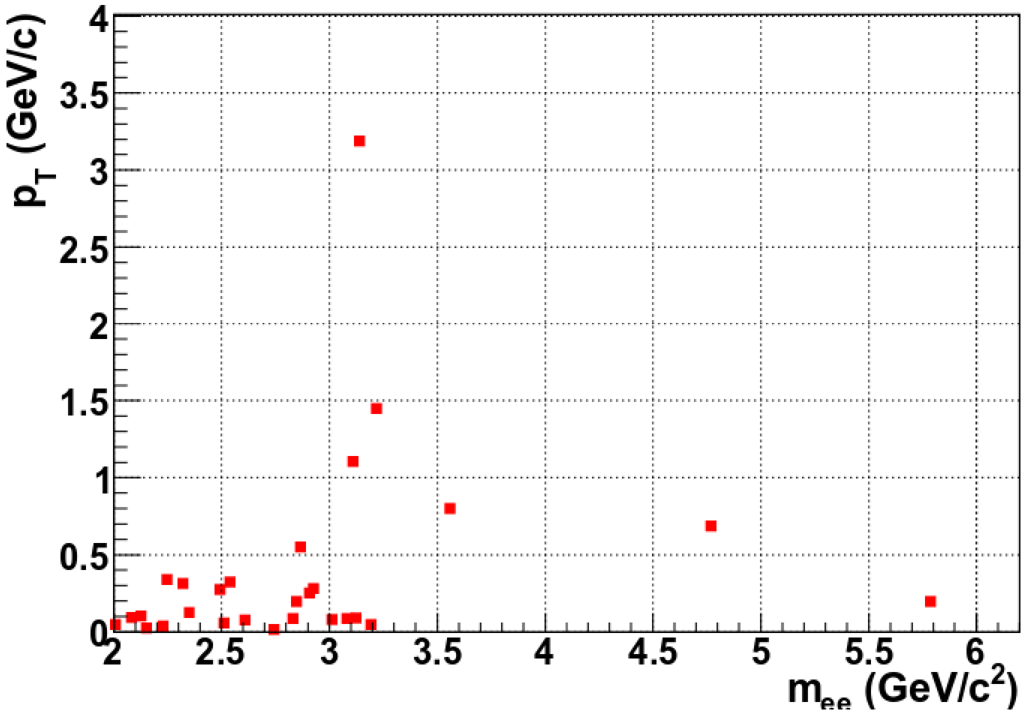


Figure 2.2: Scatter plot of $e^+e^-$ invariant mass on $p_T$ [16].

From the extracted yields were calculated cross sections for photoproduction at mid-rapidity in UPC Au+Au collisions with forward neutron emission. For $e^+e^-$ pairs the double differential cross section is calculated as

$$\left.\frac{\mathrm{d}^2\sigma_{e^+e^-+Xn}}{\mathrm{d}y, \mathrm{d}m_{e^+e^-}}\right|_{|y|<0.35, \Delta m_{e^+e^-}} = \frac{N_{e^+e^-}}{Acc \cdot \varepsilon \cdot \varepsilon_{trigg} \cdot \mathscr{L}_{int}} \cdot \frac{1}{\Delta y} \cdot \frac{1}{\Delta m_{e^+e^-}} \tag{2.1}$$

and yields $\left.\frac{d^2\sigma_{e^+e^-+Xn}}{dy,dm_{e^+e^-}}\right|_{|y|<0.35,\Delta m_{e^+e^-}} = 6 \pm 23\,(\mathrm{stat}) \pm 16\,(\mathrm{syst})\ \mu\mathrm{b}/(\mathrm{GeV/c}^2)$ for $m_{e^+e^-} \in [2.0{,}2.8]$ GeV/c$^2$.

For J/$\psi$ the cross section is calculated as

$$\left.\frac{d\sigma_{J/\psi+Xn}}{dy}\right|_{|y|<0.35} = \frac{1}{BR} \cdot \frac{N_{J/\psi}}{Acc \cdot \varepsilon \cdot \varepsilon_{trigg} \cdot \mathcal{L}_{int}} \cdot \frac{1}{\Delta y} \tag{2.2}$$

and yields $\left.\frac{d\sigma_{J/\psi+Xn}}{dy}\right|_{|y|<0.35} = 76 \pm 31\,(\mathrm{stat}) \pm 15\,(\mathrm{syst})\ \mu\mathrm{b}$.

This result is compared with theoretical predictions in Fig. 2.3. The theoretical predictions are in good agreement with the measured cross section within the large statistical uncertainties. These uncertainties do not allow to draw a more detailed conclusions.

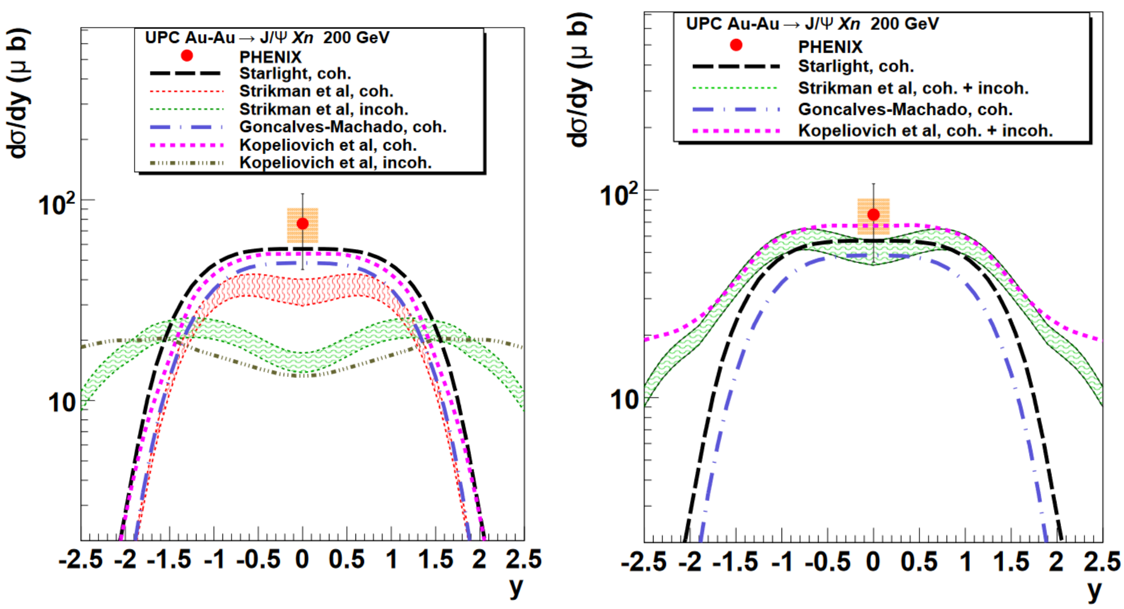


(a) (b)

Figure 2.3: Measurement results of the cross section for J/$\psi + Xn$ at mid-rapidity in UPC compared to theoretical predictions. The error bar (box) shows the statistical (systematical) uncertainties of the measurement. If possible the coherent and incoherent components of the theoretical predictions are showed separately in (a) and summed up in (b) [16].

The measured cross section can also be compared to photonucleon J/$\psi$ cross section measured in $e-p$ collisions at HERA. The results are compatible with a scaling of the cross section with the number of nucleons in gold.

## 2.2 Coherent J/$\psi$ photoproduction in ultra-peripheral PbPb collisions at $\sqrt{s_{\mathrm{NN}}}$ = 2.76 TeV with the CMS experiment

”Coherent J/$\psi$ photoproduction in ultra-peripheral PbPb collisions at $\sqrt{s_{NN}}$ = 2.76 TeV with the CMS experiment” [26] is a paper by the CMS collaboration.

The data analysed in this paper were acquired by the CMS detector at the LHC in the 2011 PbPb run, corresponding to an integrated luminosity of 159 $\mu$b$^{-1}$. The events are selected by a UPC trigger with the following conditions:

1. Energy deposit in either of the Zero Degree Calorimeters (ZDCs) consistent with at least one neutron.
2. No activity in at least one of the Beam Scintillator Counters (BSCs).
3. At least one single muon with $p_T$ over threshold.
4. At least one track in the pixel detector.

In order to suppress beam-gas interactions and non-UPC events the following offline cuts are imposed:

1. The z position of the primary vertex is required to be within 25 cm of the beam spot centre.
2. The length of the pixel clusters must be consistent with tracks originating from this vertex. This removes beam background events which produce elongated clusters in the pixel detector.
3. The time difference between hits in the two BSCs has to be smaller then 20 ns with respect to the mean flight time between them (73 ns). This requirement removes beam-halo events.

As mentioned above, one of the requirements of the UPC trigger is the presence of at least one neutron in either of the ZDCs. The events analysed in this paper are classified based on the number of neutrons deposited in the ZDCs. The detectors have a resolution of about 20% for single neutron detection in PbPb collisions at $\sqrt{s_{NN}}$ = 2.76 TeV and this allows CMS to obtain a good resolution of zero, one ore multiple neutron events.

The coherent J/$\psi$ cross section is measured with events which have at least one neutron on one side of the interaction point and no neutron on the other side ($\mathrm{X_n0_n}$). This is a subset of the triggered events and it is well suited for rejection of non-UPC events due to its asymmetric shape. Apart from this break-up mode also events in the $\mathrm{X_nX_n}$, $\mathrm{1_n0_n}$ and $\mathrm{1_n1_n}$ break-up modes are recorded.

In addition to the ZDC requirement, two other conditions are applied to reject non-UPC events:

1. Events must have exactly two reconstructed tracks.
2. The Hadronic Forward (HF) calorimeter cell with the largest energy deposit is required to be below 3.85 GeV. This requirement ensures that the HF energy is consistent with a photon-induced event.

The recorded muon tracks have to lie within the phase space region $1.2 < |\eta| < 2.4$ and $1.2 < p_T < 1.8$ GeV to ensure good data quality. Furthermore, to ensure good identification and track reconstruction the single muons are required to pass the following criteria:

1. More then four hits in the tracker and at least one is required to be in the pixel layer.
2. Track fit with $\chi^2$ per degree of freedom less than three.
3. Transverse (longitudinal) impact parameter less then 0.3 (20) cm from the measured vertex.
4. Dimuon $p_T < 1.0$ GeV, rapidity interval $1.8 < |y| < 2.3$ and mass interval $2.6 < m(\mu^+\mu^-) < 3.5$ GeV.

No like-sign pairs are found after these selections. The muon quality criteria, after all other selections, reject only one event from 518.

The acceptance and efficiency corrections are calculated from a STARLIGHT Monte Carlo simulation folded with the full CMS simulation and reconstruction software.

With all the selection criteria mentioned above the $p_T$ and invariant mass distributions are simultaneously fitted to extract the number of coherent J/$\psi$, incoherent J/$\psi$ and $\gamma + \gamma \rightarrow \mu^+\mu^-$ events. The fit uses an unbinned maximum likelihood algorithm. The shapes of the $p_T$ distributions are determined from the STARLIGHT MC. The invariant mass fit uses a Crystal Ball model for the coherent and incoherent J/$\psi$ and a second-order polynomial to describe the background continuum from $\gamma+\gamma \rightarrow \mu^+\mu^-$ events. The fit constrains the number of coherent J/$\psi$, incoherent J/$\psi$ and $\gamma+\gamma \rightarrow \mu^+\mu^-$ events to be the same in both the $p_T$ and invariant mass distributions. The $p_T$ and invariant mass fit of the $\mathrm{X_n0_n}$ break-up class can be seen in Fig. 2.4.

For events with $p_T < 0.15$ GeV (corresponding to coherent J/$\psi$ production) in the rapidity interval $1.8 < \eta < 2.3$ the fit yields $207 \pm 18$ (stat) coherent J/$\psi$ candidates, $75 \pm 13$ (stat) for incoherent J/$\psi$ candidates (corresponding to events with $p_T > 0.15$ GeV) and $75 \pm 13$ (stat) for $\gamma+\gamma$ background.

In addition, the data sample is studied in terms of two cases: i) neutrons emitted with the same rapidity sign as the J/$\psi$ or ii) neutrons emitted with the opposite rapidity sign

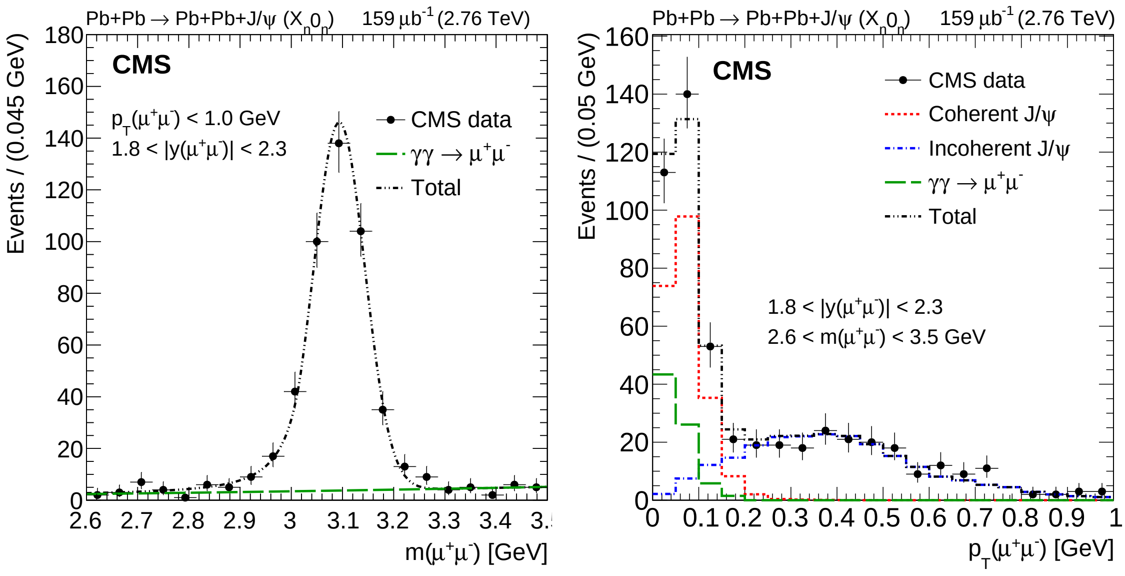


Figure 2.4: Results of the simultaneous fit to dimuon invariant mass (a) and $p_T$ (b) spectrums for the $X_n0_n$ break-up class. Only statistic uncertainties are shown and the data are not corrected by acceptance and efficiencies. [26].

than the J/$\psi$. This study for the coherent case shows the same number of events in the two classes (within statistical uncertainties), suggesting that the J/$\psi$ photoproduction and the neutron emission are independent processes. On the other hand, for the incoherent case most of the events have the neutrons and the J/$\psi$ with the same rapidity sign. This suggests that the low-$x$ and high-$x$ contributions are decoupled and can be more easily observed for the incoherent case.

In the $X_n0_n$ break-up mode the coherent J/$\psi$ photoproduction cross section for the dimuon channel is calculated as

$$\frac{\mathrm{d}\sigma^{\mathrm{coh}}_{X_n0_n}}{\mathrm{d}y}(\mathrm{J}/\psi) = \frac{N^{\mathrm{coh}}_{X_n0_n}}{\mathcal{B}(\mathrm{J}/\psi \to \mu^+\mu^-)\,\mathcal{L}_{\mathrm{int}}\,\Delta y\,(A\,\varepsilon)^{\mathrm{J}/\psi}}, \tag{2.3}$$

where $\mathcal{B}(\mathrm{J}/\psi \to \mu^+\mu^-) = 5.96 \pm 0.03(\mathrm{syst})\%$ is the branching ratio, $\mathcal{L}_{\mathrm{int}} = 159 \pm 8(\mathrm{syst})\mu\mathrm{b}^{-1}$ is the integrated luminosity, $\Delta y = 1$ is the size of the rapidity bin and $(A\,\varepsilon)^{\mathrm{J}/\psi} = 5.9 \pm 0.5(\mathrm{stat})\%$ is the acceptance times efficiency correction factor. $N^{\mathrm{coh}}_{X_n0_n}$ is the coherent J/$\psi$ yield for prompt J/$\psi$ candidates with $p_T < 0.15$ GeV and it is given by

$$N^{\mathrm{coh}}_{X_n0_n} = \frac{N_{\mathrm{yield}}}{1+f_D}, \tag{2.4}$$

where $N_{\mathrm{yield}}$ is the coherent J/$\psi$ yield extracted from Fig. 2.4 and $f_D$ is the feed-down ratio from coherent $\psi(2S) \to \mathrm{J}/\psi + X$ decay. There are not enough data to perform a coherent $\psi(2S)$ analysis, so the feed-down ratio has to be calculated from MC simulations. STARLIGHT is used to simulate coherent $\psi(2S)$ events and PYTHIA is used to simulate the decay into J/$\psi$. This procedure gives $f_D = 0.018 \pm 0.011$(theo), together with $N_{yield} = 207 \pm 18$(stat), mentioned above, the coherent J/$\psi$ yield is calculated to be $N^{\text{coh}}_{X_n0_n} = 203 \pm 18$(stat). Finally, the coherent J/$\psi$ photoproduction cross section in the $X_n0_n$ break-up mode is $\frac{\mathrm{d}\sigma^{\text{coh}}_{X_n0_n}}{\mathrm{dy}}(\mathrm{J}/\psi) = 0.36 \pm 0.04(\text{stat}) \pm 0.04(\text{syst})$ mb.

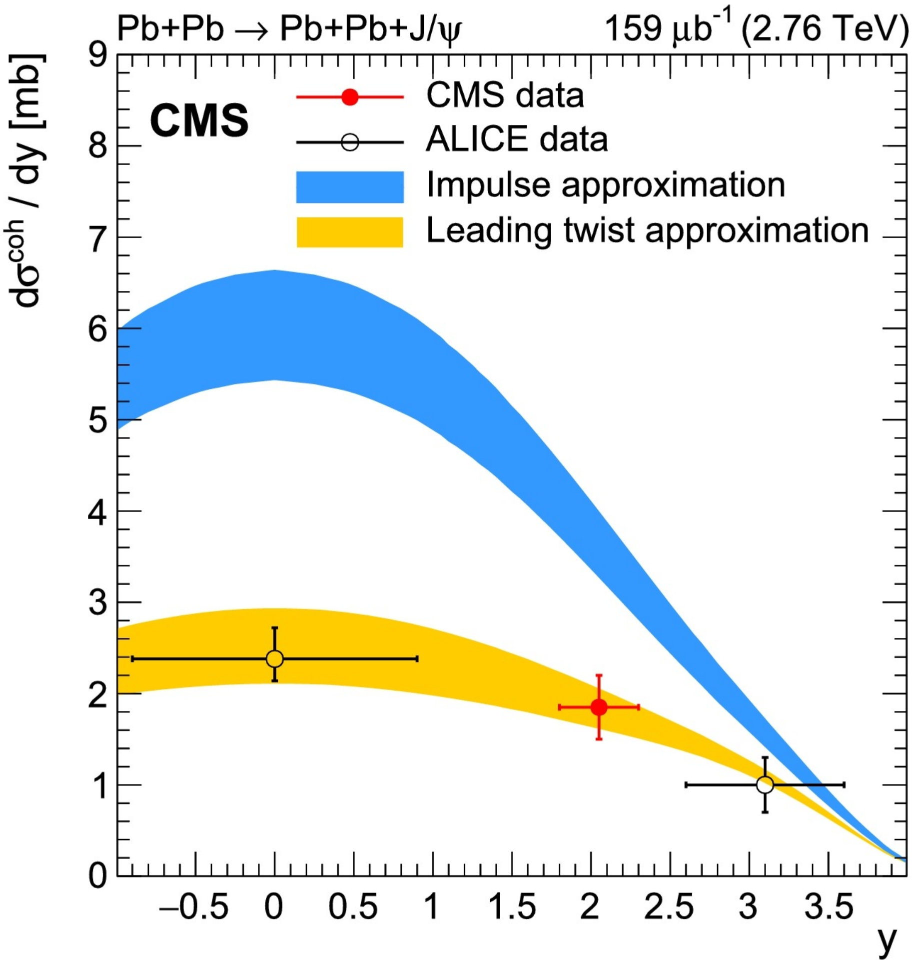


Figure 2.5: Differential coherent J/$\psi$ cross section dependence on rapidity measured in PbPb UPC at $\sqrt{s_{NN}}$ = 2.76 TeV by ALICE and CMS. The vertical error bars include the statistical and systematic uncertainties added in quadrature, and the horizontal bars represent the range of the measurements in y. The impulse approximation and the leading twist approximation calculations are also shown [26].

In order to be able to compare this result with the the theoretical predictions and results from the ALICE collaboration, the total coherent J/$\psi$ cross section has to be calculated from the $X_n 0_n$ break-up mode. This is done with the STARLIGHT MC generator, which can simulate the various break-up modes. The total coherent J/$\psi$ cross section is then $\frac{\mathrm{d}\sigma^{\mathrm{coh}}}{\mathrm{d}y}(\mathrm{J}/\psi) = 1.82 \pm 0.22(\mathrm{stat}) \pm 0.20(\mathrm{syst}) \pm 0.19(\mathrm{theo})$ mb. In Fig. 2.5 the CMS and ALICE results are compared to theoretical calculations based on the impulse and leading twist approximations.

The leading twist approximation is a calculation at the partonic level that includes a mechanism for nuclear gluon shadowing and it is in good agreement with the data. The impulse approximation neglects all nuclear effects and it overpredicts the CMS result by more then three standard deviations.

## 2.3 Measurement of an excess in the yield of J/$\psi$ at very low $p_\mathrm{T}$ in Pb–Pb collisions at $\sqrt{s_{\mathrm{NN}}}$ = 2.76 TeV

"Measurement of an excess in the yield of J/$\psi$ at very low $p_T$ in Pb–Pb collisions at $\sqrt{s_{NN}}$ = 2.76 TeV" [27] is a paper by the ALICE collaboration and it presents the first measurement of an excess (with respect to the hadroproduction expectation) in the J/$\psi$ yield at very low transverse momentum ($p_T < 0.3$ GeV/c) for peripheral Pb–Pb collisions. It is plausible that this excess is caused by the coherent photoproduction of J/$\psi$. However, it had never been observed in non-UPC collisions and it raises several questions, e.g. how the break-up of the nuclei influences the coherence requirements.

The J/$\psi$ was measured in the forward region via its dimuon decay channel. The data used in this analysis were measured by the ALICE detector at the LHC and corresponds to approximately $17 \times 10^6$ minimum-bias (MB) $\mu\mu$ triggered Pb–Pb collisions, which translates into an integrated luminosity of $\mathscr{L}_{\mathrm{int}} \approx 70\ \mu\mathrm{b}^{-1}$. The Silicon Pixel Detector (SPD) provides the coordinates of the primary vertex. The minimum-bias (MB) trigger requires a signal in both of the V0 detectors. The dimuon opposite-sign trigger, used in this analysis, requires at least one pair of opposite-sign track segments in the muon spectrometer triggering system, each with a $p_T$ above the 1 GeV/c threshold. The beam and electromagnetic background were reduced by V0 and Zero Degree Calorimeter (ZDC) timing information and by a minimum energy level required in the neutron ZDC (ZNA, ZNC). The energy thresholds were $\sim$ 450 GeV and $\sim$ 500 GeV for the ZNA and ZNC, respectively. This corresponds to an energy threshold approximately three standard deviations below the energy deposited by a 1.38 TeV neutron. The centrality was determined from a fit to the V0 amplitude distribution. The 90% most central collision were used for this analysis and for these the MB trigger was fully efficient. For each centrality class, the average number of participant nucleons $\langle N_{\mathrm{part}} \rangle$ and average value of the nuclear overlap function were calculated from a Glauber model.

In Fig. 2.6 the raw $p_T$ distribution of opposite sign dimuons (without combinatorial background subtraction) can be seen for the invariant mass range $2.8 < m_{\mu^+\mu^-} < 3.4$ GeV/c$^2$ and the 70-90% centrality class.

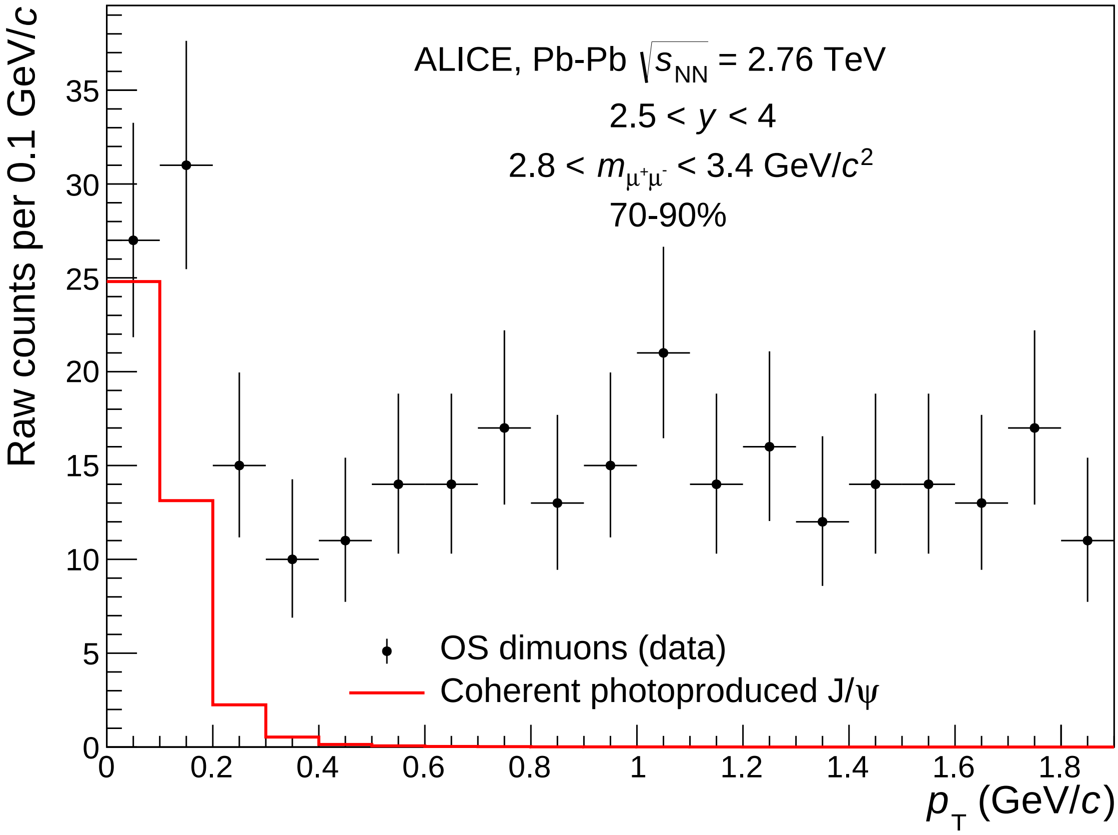


Figure 2.6: Opposite sign dimuon $p_T$ distribution for the invariant mass range $2.8 < m_{\mu^+\mu^-} < 3.4$ GeV/c$^2$ and the 70-90% centrality class. Vertical bars represent statistical uncertainties. The red line represents the $p_T$ distribution of coherently produced J/$\psi$ in Pb–Pb UPC as predicted by the STARLIGHT MC generator and folded with the muon spectrometer response function [27].

There is a significant excess of dimuons at very low $p_T$ in this centrality class, such an excess has not been observed in the like-sign dimuon $p_T$ distribution, neither in proton-proton collisions.

To extract the number of J/$\psi$ the invariant mass distribution was fitted with a Crystal Ball function or a pseudo-Gaussian function describing the signal. The tails for the J/$\psi$ signal functions were fixed using MC simulations and two or three functions were considered to describe the background. In addition, the fit range and the bin width were varied to check the impact on the signal extraction process.

In Fig. 2.7 a typical invariant mass fit can be seen for the $p_T$ range 0-0.3 GeV/c and centrality classes 0-10% (top) and 70-90% (bottom). The extracted number of J/$\psi$ is the average of the results from making every combination of all the signal and background

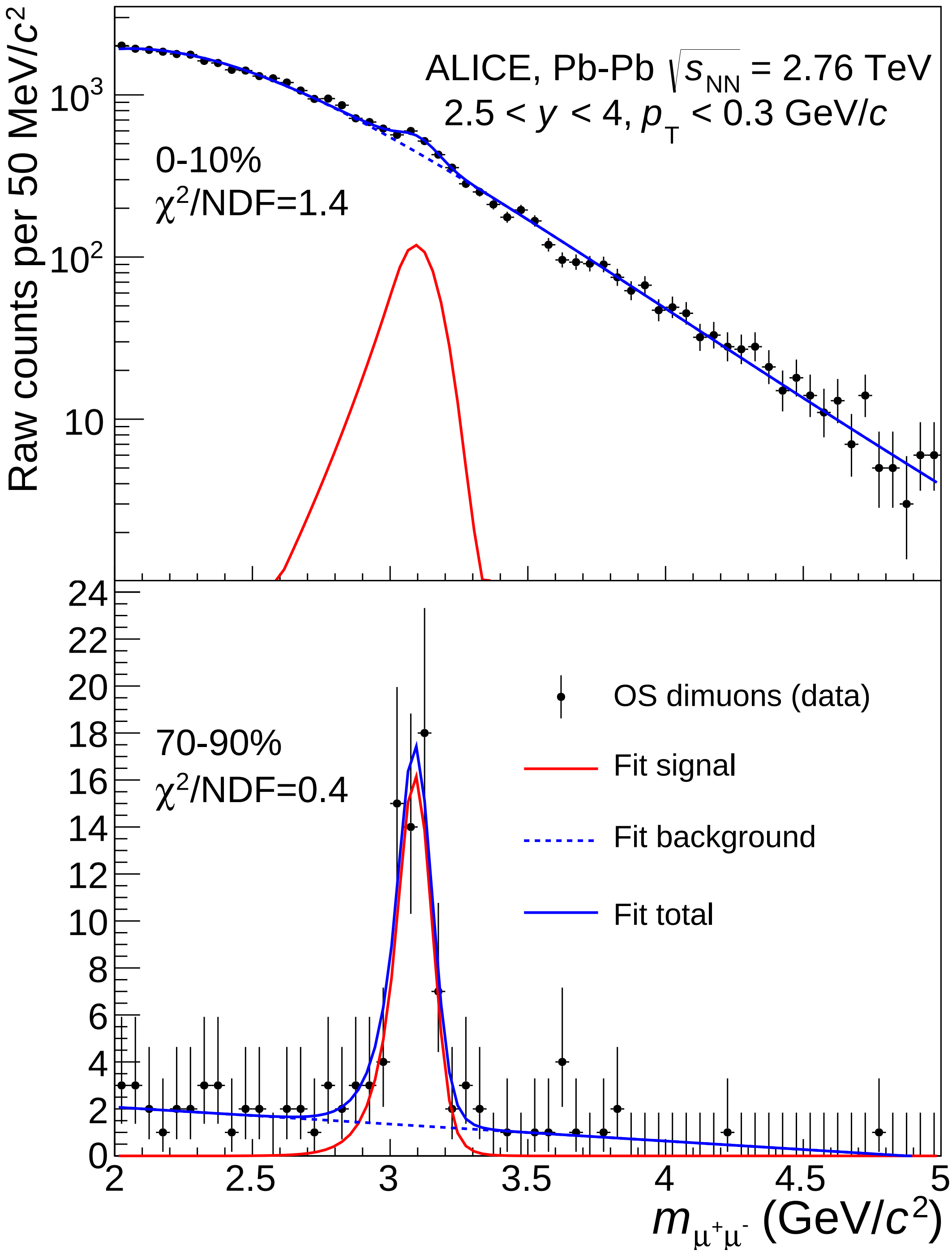


Figure 2.7: Opposite sign dimuon invariant mass distribution for $p_T$ range 0-0.3 GeV/c and centrality classes 0-10% (top) and 70-90% (bottom). Vertical bars represent statistical uncertainties [27].

shape functions as well as different fitting ranges. The systematic uncertainties are obtained from the RMS of the results.

In each centrality class and $p_T$ range the $R_{AA}$ was obtained using this formula:

$$R_{\mathrm{AA}}^{\mathrm{h\ J}/\psi} = \frac{N_{\mathrm{AA}}^{\mathrm{J}/\psi}}{\mathrm{BR}_{\mathrm{J}/\psi\to\mathrm{l^+l^-}} \times N_{\mathrm{events}} \times (\mathcal{A}\times\varepsilon)_{\mathrm{AA}}^{\mathrm{h\ J}/\psi} \times \langle \mathrm{T_{AA}} \rangle \times \sigma_{\mathrm{pp}}^{\mathrm{h\ J}/\psi}}, \tag{2.5}$$

where $N_{\mathrm{AA}}^{\mathrm{J}/\psi}$ is the measured number of J/$\psi$, $\mathrm{BR}_{\mathrm{J}/\psi\to\mathrm{l^+l^-}}$ is the branching ratio, $N_{\mathrm{events}}$ is the number of MB events used for normalisation, $(\mathcal{A}\times\varepsilon)_{\mathrm{AA}}^{\mathrm{h\ J}/\psi}$ is the acceptance and efficiency (assuming pure hadroproduction), $\langle \mathrm{T_{AA}} \rangle$ is the average nuclear overlap function and $\sigma_{\mathrm{pp}}^{\mathrm{h\ J}/\psi}$ is the proton-proton inclusive J/$\psi$ production cross section.

In Fig. 2.8 the J/$\psi$ $R_{AA}$ dependence on $\langle N_{\mathrm{part}} \rangle$ is shown. There is a strong increase in the $R_{AA}$ at low $p_T$ (0-0.3 GeV/c) for the most peripheral Pb–Pb collisions, which is not predicted by any of the transport models that described well the previous measurements.

As mentioned earlier, a possible explanation of this excess is J/$\psi$ photoproduction. At LHC energies the photoproduction cross section is comparable to the hadronic J/$\psi$ cross section. Also, the shape of the $p_T$ distribution, where the excess is observed, is similar to that of coherent J/$\psi$ photoproduction. Thus, assuming that coherent J/$\psi$ photoproduction is the cause of this excess, the corresponding cross section can be calculated using Eq. 2.3 and Eq. 2.4. For the 70-90% centrality class the cross section per unit rapidity is calculated to be 59 $\pm$ 11 (stat)$^{+7}_{-10}$ (uncor. syst) $\pm$ 8 (cor. syst) $\mu$b.

In Pb–Pb UPC at $\sqrt{s_{NN}} = 2.76$ TeV the incoherent yield in the 0.3-1 GeV/c $p_T$ range should be about 30% of the coherent yield in the 0-0.3 GeV/c $p_T$ range. If the behaviour is the same in peripheral collisions, the expected contribution to the total number of J/$\psi$ from the incoherent J/$\psi$ photoproduction should amount to 23% (4%) in the 70-90% (50-70%) centrality class in the 0.3-1 GeV/c $p_T$ range. Unfortunately the significance of the analysed data sample does not allow to confirm the presence of the incoherent contribution in this $p_T$ range.

The probability of a coincidence of a MB collision and a coherent J/$\psi$ photoproduction in UPC satisfying the dimuon trigger in the same bunch crossing has been calculated. For the analysed data sample only one random coincidence is expected for the full centrality range.

A calculation was made to determined the expected J/$\psi$ photoproduction cross section. As a rough estimate all the protons (charges) in the source and all the nucleons in the target were considered to contribute to the cross section as in UPC, even though the fact that the nuclei also undergoes a hadronic interaction may influence the coherence conditions. Two different models were used for the calculation, a vector dominance model and a perturbative QCD model. Both of them result in an approximately 40 $\mu$b cross section for the 70-90% centrality class, which is of the same order as the measured value.

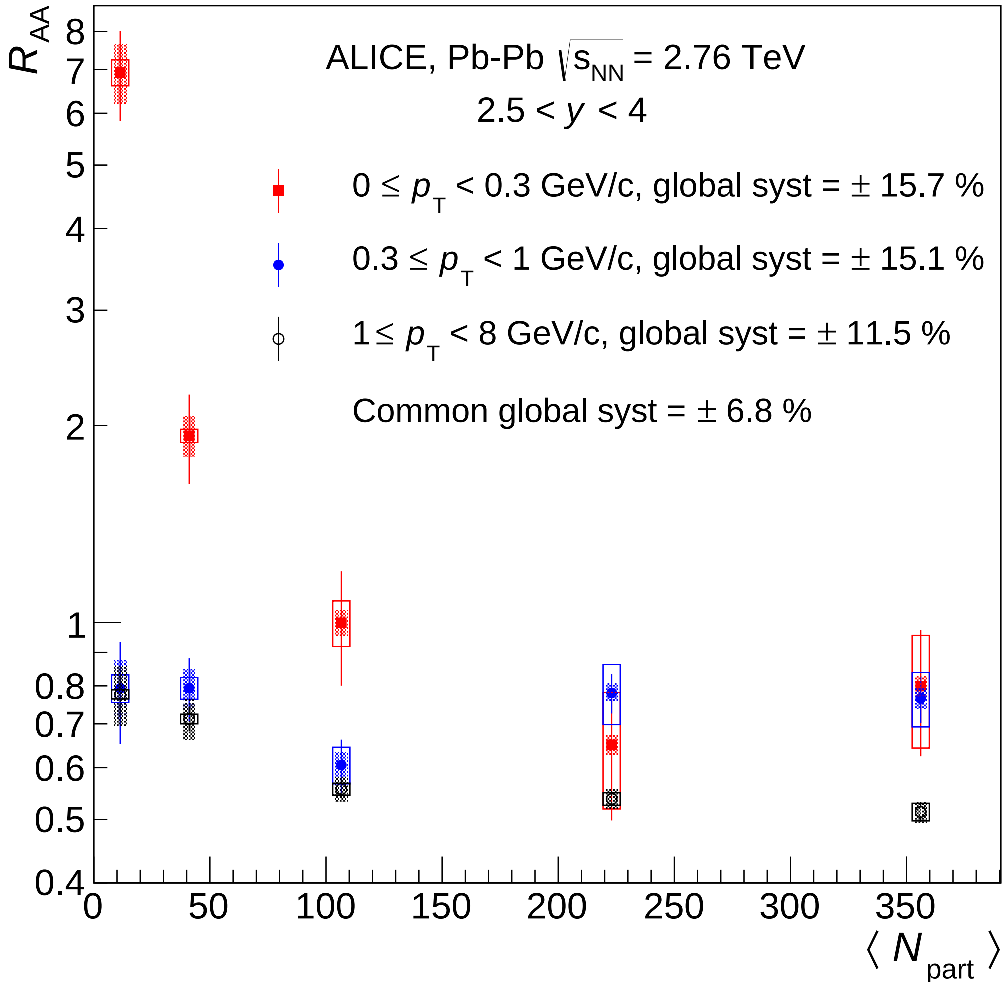


Figure 2.8: The $R_{AA}$ for J/$\psi$ production as a function of $\langle N_{\text{part}} \rangle$ fro three $p_T$ ranges in Pb–Pb collisions at $\sqrt{s_{NN}} = 2.76$ TeV. [27].

For the most peripheral collisions only a few nucleons ($N_{\text{part}} \approx 11$) interact hadronically, hence the interaction is close to ultra-peripheral and the comparison of the cross section is reasonable. A proposed, but not investigated, hypothesis is that only the spectator nucleons would interact coherently with the photon. In this case, the $p_T$ distribution would get wider with increasing centrality.

# Chapter 3

# Data analysis

The analysis focuses on measuring the $J/\psi$ decay in the dimuon decay chanel in the forward rapidity region.

In the coherent $J/\psi$ photoproduction analysis one of the key steps is to determine the coherent contribution to the overall $J/\psi$ signal. One of the ways in which this can be achieved is to fit the $p_T$ spectrum by MC distribution templates, which correspond to all involved processes. This method is the main focus of this chapter.

## 3.1 Data

The analysed data were recorded during the LHC Run 2 in Pb+Pb ultra-peripheral collisions at $\sqrt{s_{NN}} = 5.02$ TeV with ALICE, more specifically by the forward muon calorimeter. Within the analysis, Monte Carlo data were used to extract the contributions of different dimuon production processes and they served to test the analysis procedure as well.

The Monte Carlo data were simulated with the STARLIGHT MC generator and folded with the ALICE detector response. The following processes were considered coherent $J/\psi$ photoproduction, incoherent $J/\psi$ photoproduction, feed-down contribution from coherent $\psi(2S)$ photoproduction, feed-down contribution from incoherent $\psi(2S)$ photoproduction and $\gamma\gamma$ background events producing dimuons.

Different parts of the MC data sets were used for the signal extraction process and different for the testing of the analysis procedure.

## 3.2 Models for signal extraction

### 3.2.1 Transverse momentum spectrum

From the STARLIGHT generated Monte Carlo data samples were created RooFit Probability Density Function (PDF) templates for each of the respective processes to be able to fit the $p_T$ spectrum of real data.

For the incoherent $J/\psi$ production with proton dissociation there was no MC sample and therefore the following parametrisation was used [28]

$$\frac{d\sigma}{dt} = N_{pd}(1+(b_{pd}/n_{pd})|t|)^{-n_{pd}}, \tag{3.1}$$

where $N_{pd}$ is the normalisation parameter, $t$ is the transverse momentum squared, $n_{pd} = 3.56$ and $b_{pd} = 1.7\ \mathrm{GeV}^{-2}$, which are values based on [28].

The fitting model for the $p_T$ fit consists of a sum of the coherent $J/\psi$, incoherent $J/\psi$, incoherent $J/\psi$ with proton dissociation, feed down from coherent $\psi(2S)$, $\gamma\gamma$ background templates and the incoherent $J/\psi$ production with proton dissociation distribution from Eq. 3.1. The feed-down contribution from the incoherent $\psi(2S)$ photoproduction was found to be negligible and therefore was omitted from the fitting model.

### 3.2.2 Invariant mass spectrum

To describe the $J/\psi$ signal in the invariant mass spectrum, the Crystal Ball function [29] was used.

$$\begin{aligned} f(x;\alpha,n,\bar{x},\sigma) &= e^{-\frac{1}{2}\left(\frac{x-\bar{x}}{\sigma}\right)^2} && \text{for} \quad \frac{x-\bar{x}}{\sigma} > -\alpha \\ &= \left(\frac{n}{|\alpha|}\right)^n e^{-\frac{|\alpha|^2}{2}} \left(\frac{n}{|\alpha|} - |\alpha| - \frac{x-\bar{x}}{\sigma}\right)^{-n} && \text{for} \quad \frac{x-\bar{x}}{\sigma} \leq -\alpha \end{aligned} \tag{3.2}$$

It is composed from a Gaussian core with a power law times an exponential tail, which is descried by the parameters $\alpha$ and $n$.

The dimuon background in the invariant mass spectrum was described using the following formula [30].

$$f(x;\lambda,t,a_1,a_2,a_3) = e^{\lambda x}[1+a_1(x-t)^2+a_2(x-t)^3+a_3(x-t)^4] \qquad \text{for} \quad x \leq t \tag{3.3}$$

The simple exponential model for background is modified by a fourth order polynomial, which mainly manifests in the smaller invariant mass region to describe the decrease in the detector efficiency.

## 3.3 Results

Global cuts applied to all data were that the dimoun pair had rapidity ($-4 < y < -2.5$) and $p_T$ ($p_T < 3$ GeV/c). For the transverse momentum distributions a cut on the J/$\psi$ invariant mass window was done (2.5 GeV/c$^2$ $< m <$ 3.5 GeV/c$^2$).

The $p_T$ fit to real data with its correlation matrix can be seen in Fig. 3.1 and the number of events for the individual processes can be seen in Tab. 3.1.

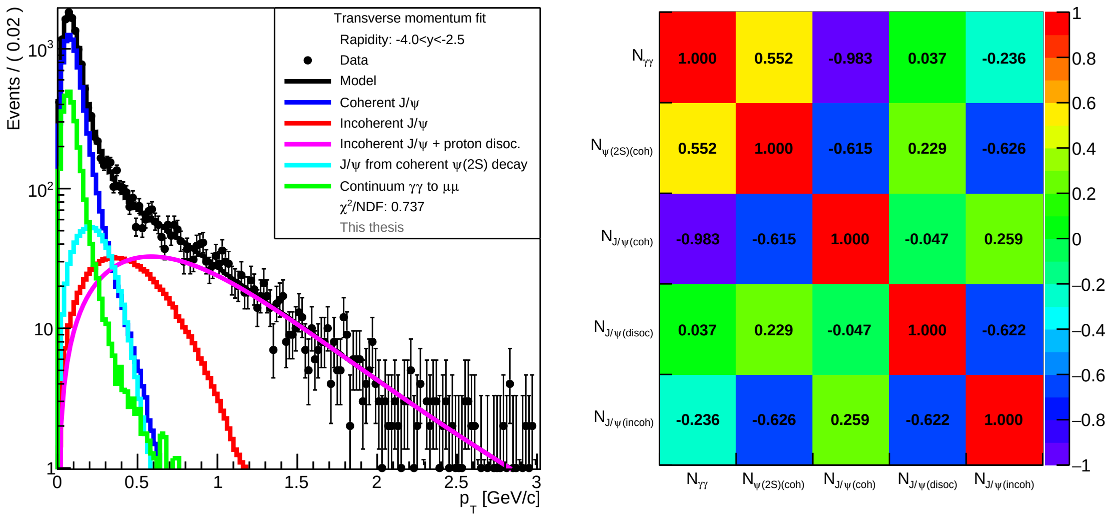


Figure 3.1: Fit to the transverse momentum spectrum of real data with a correlation matrix.

| Process | N$_{fit}$ | $\sqrt{N_{fit}}$ | $\sigma_{N_{fit}}$ |
|---|---|---|---|
| N$_{J/\psi(coh)}$ | 8218 | 91 | 690 |
| N$_{J/\psi(incoh)}$ | 954 | 31 | 105 |
| N$_{\psi(2S)(coh)}$ | 782 | 28 | 131 |
| N$_{\gamma\gamma}$ | 2834 | 53 | 632 |
| N$_{J/\psi(disoc)}$ | 1926 | 44 | 71 |

Table 3.1: The number of events for given process, its square root (expected statistical uncertainty) and the standard deviation from the $p_T$ fit to real data.

Even thought the $\chi^2$ value of the fit is good and the fit optically seems good, there is a very strong anticorrelation between the coherent J/$\psi$ production contribution and the $\gamma\gamma$ background contribution. This transfers to the standard deviations of the estimated number of events. The expected value for a statistical error is the square root of the original value. From Tab. 3.1 is clear that the standard deviations are significantly larger.

The same analysis was done on Monte Carlo data in Fig. 3.2 with the number of events in Tab. 3.2.

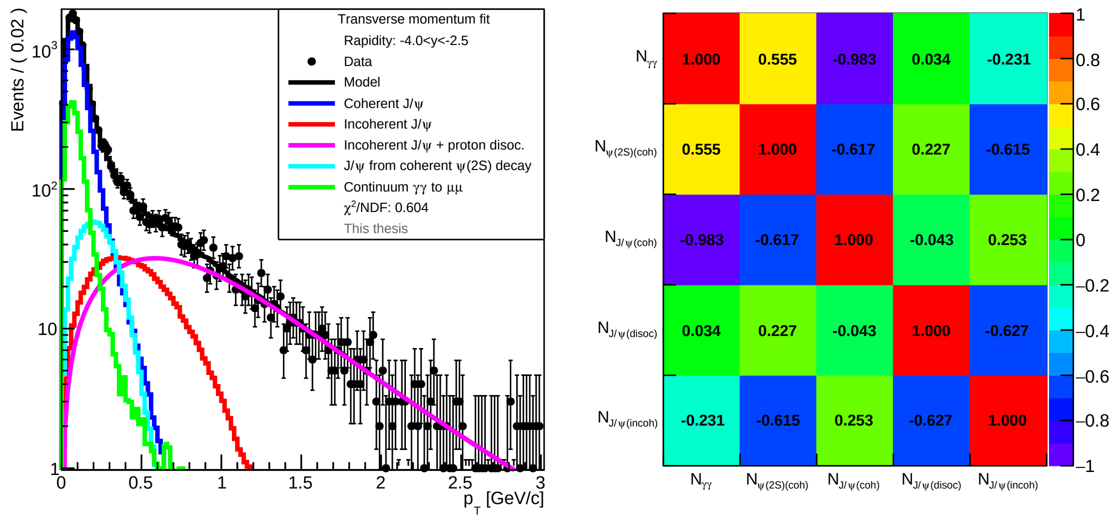


Figure 3.2: Fit to the transverse momentum spectrum of Monte Carlo data with a correlation matrix.

| **Process** | **#entries** | $N_{fit}$ | $\sqrt{N_{fit}}$ | $\sigma_{N_{fit}}$ |
|---|---|---|---|---|
| $N_{J/\psi(coh)}$ | 8241 | 8652 | 93 | 693 |
| $N_{J/\psi(incoh)}$ | 959 | 961 | 31 | 105 |
| $N_{\psi(2S)(coh)}$ | 781 | 855 | 29 | 130 |
| $N_{\gamma\gamma}$ | 2844 | 2397 | 49 | 633 |
| $N_{J/\psi(disoc)}$ | 1926 | 1885 | 43 | 71 |

Table 3.2: The number of events for given process, its square root (expected statistical uncertainty) and the standard deviation from the $p_T$ fit to Monte Carlo data.

When the fitted values are compared with the true input values, it can be seen that there are events from the $\gamma\gamma$ background, which are falsely identified as the coherent J/$\psi$ events.

The fit behaviour is the same as for real data, therefore the same effect is expected to be present there as well. To examine this behaviour more closely a systematic analysis in which every contribution is one by one fixed to the input value was conducted.

The $p_T$ fit to Monte Carlo data and its correlation matrix with the coherent $J/\psi$ contribution fixed can be seen in Fig. 3.3 and the number of events for the individual processes can be seen in Tab. 3.3.

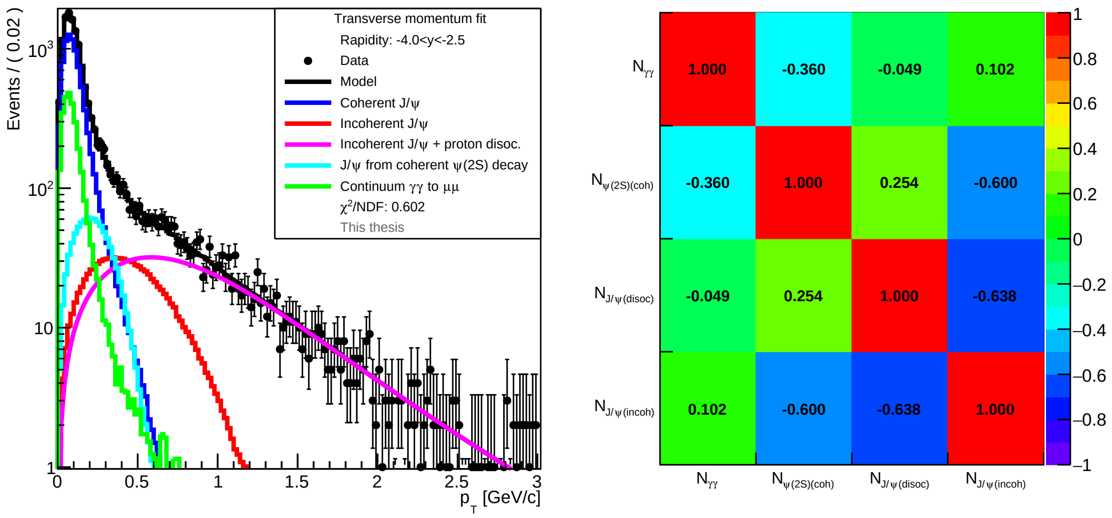


Figure 3.3: Fit to the transverse momentum spectrum of Monte Carlo data with a correlation matrix. The coherent $J/\psi$ contribution is fixed in the fit.

| **Process** | **#entries** | $N_{fit}$ | $\sqrt{N_{fit}}$ | $\sigma_{N_{fit}}$ |
|---|---|---|---|---|
| $N_{J/\psi(coh)}$ | 8241 | 8241 | fixed | fixed |
| $N_{J/\psi(incoh)}$ | 959 | 945 | 31 | 101 |
| $N_{\psi(2S)(coh)}$ | 781 | 902 | 30 | 103 |
| $N_{\gamma\gamma}$ | 2844 | 2766 | 53 | 117 |
| $N_{J/\psi(disoc)}$ | 1926 | 1887 | 43 | 71 |

Table 3.3: The number of events for given process, its square root (expected statistical uncertainty) and the standard deviation from the $p_T$ fit to Monte Carlo data with the coherent $J/\psi$ contribution fixed.

With the coherent contribution fixed, most of the $\gamma\gamma$ events are classified correctly and the standard deviation of the $N_{\gamma\gamma}$ is significantly smaller then before but still a factor of two larger than expected.

The $p_T$ fit to Monte Carlo data and its correlation matrix with the incoherent J/$\psi$ contribution fixed can be seen in Fig. 3.4 and the number of events for the individual processes can be seen in Tab. 3.4.

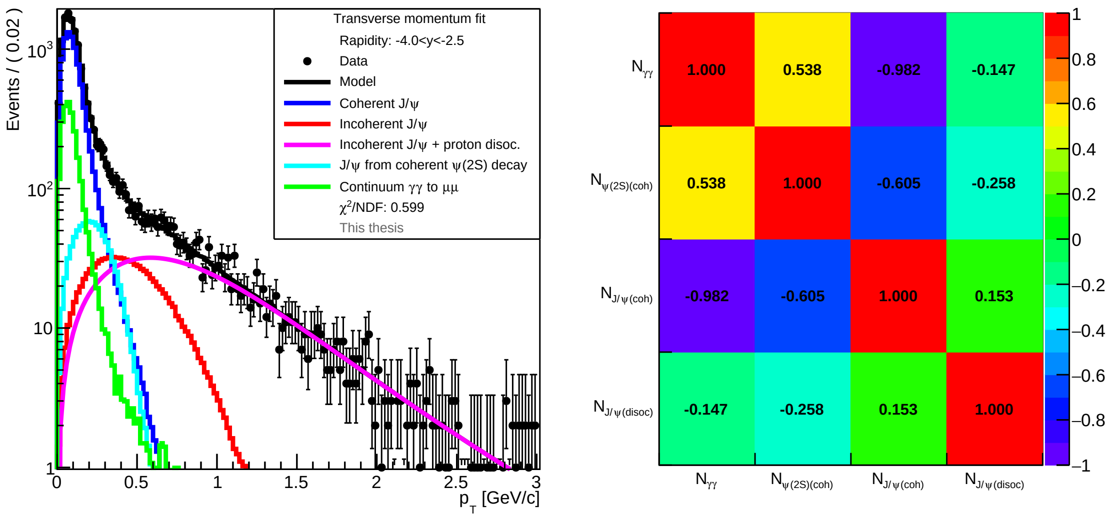


Figure 3.4: Fit to the transverse momentum spectrum of Monte Carlo data with a correlation matrix. The incoherent J/$\psi$ contribution is fixed in the fit.

| **Process** | **#entries** | $N_{fit}$ | $\sqrt{N_{fit}}$ | $\sigma_{N_{fit}}$ |
|---|---|---|---|---|
| $N_{J/\psi(coh)}$ | 8241 | 8649 | 93 | 670 |
| $N_{J/\psi(incoh)}$ | 959 | 959 | fixed | fixed |
| $N_{\psi(2S)(coh)}$ | 781 | 857 | 29 | 103 |
| $N_{\gamma\gamma}$ | 2844 | 2398 | 49 | 617 |
| $N_{J/\psi(disoc)}$ | 1926 | 1886 | 43 | 55 |

Table 3.4: The number of events for given process, its square root (expected statistical uncertainty) and the standard deviation from the $p_T$ fit to Monte Carlo data with the incoherent J/$\psi$ contribution fixed.

Fixing the incoherent J/$\psi$ contribution does not yield any significant changes in the fit behaviour. Only the standard deviation in the number of dissociative events slightly decreases, which is caused by the fact that dissociative contribution has a correlation factor of -0.622 with the incoherent J/$\psi$ contribution.

The $p_T$ fit to Monte Carlo data and its correlation matrix with the coherent $\psi(2S)$ contribution fixed can be seen in Fig. 3.5 and the number of events for the individual processes can be seen in Tab. 3.5.

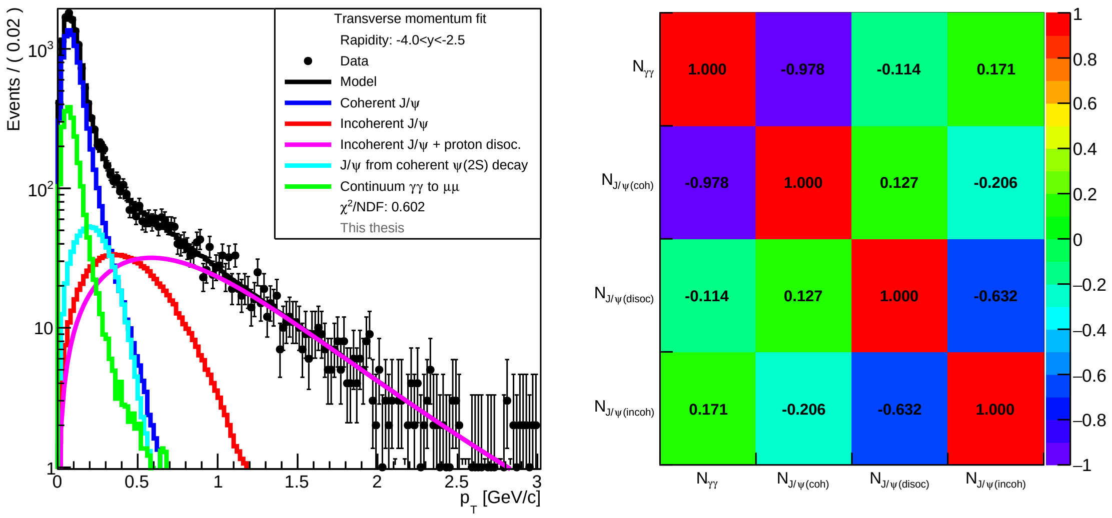


Figure 3.5: Fit to the transverse momentum spectrum of Monte Carlo data with a correlation matrix. The coherent $\psi(2S)$ contribution is fixed in the fit.

| **Process** | **#entries** | $N_{fit}$ | $\sqrt{N_{fit}}$ | $\sigma_{N_{fit}}$ |
|---|---|---|---|---|
| $N_{J/\psi(coh)}$ | 8241 | 8898 | 94 | 546 |
| $N_{J/\psi(incoh)}$ | 959 | 998 | 32 | 82 |
| $N_{\psi(2S)(coh)}$ | 781 | 781 | fixed | fixed |
| $N_{\gamma\gamma}$ | 2844 | 2193 | 47 | 528 |
| $N_{J/\psi(disoc)}$ | 1926 | 1876 | 43 | 69 |

Table 3.5: The number of events for given process, its square root (expected statistical uncertainty) and the standard deviation from the $p_T$ fit to Monte Carlo data with the coherent $\psi(2S)$ contribution fixed.

Fixing the coherent $\psi(2S)$ feed-down contribution makes the flow of events from the $\gamma\gamma$ background to the coherent J$/\psi$ production even higher.

The $p_T$ fit to Monte Carlo data and its correlation matrix with the $\gamma\gamma$ background contribution fixed can be seen in Fig. 3.6 and the number of events for the individual processes can be seen in Tab. 3.6.

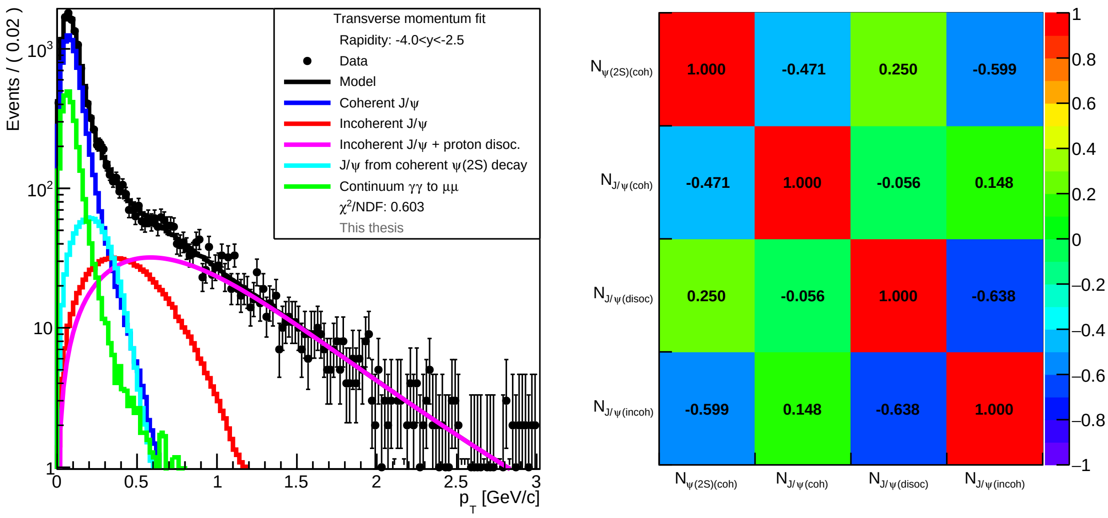


Figure 3.6: Fit to the transverse momentum spectrum of Monte Carlo data with a correlation matrix. The $\gamma\gamma$ background contribution is fixed in the fit.

| **Process** | **#entries** | $N_{fit}$ | $\sqrt{N_{fit}}$ | $\sigma_{N_{fit}}$ |
|---|---|---|---|---|
| $N_{J/\psi(coh)}$ | 8241 | 8172 | 90 | 127 |
| $N_{J/\psi(incoh)}$ | 959 | 944 | 31 | 102 |
| $N_{\psi(2S)(coh)}$ | 781 | 906 | 30 | 108 |
| $N_{\gamma\gamma}$ | 2844 | 2844 | fixed | fixed |
| $N_{J/\psi(disoc)}$ | 1926 | 1887 | 43 | 71 |

Table 3.6: The number of events for given process, its square root (expected statistical uncertainty) and the standard deviation from the $p_T$ fit to Monte Carlo data with the $\gamma\gamma$ background contribution fixed.

With the $\gamma\gamma$ background contribution fixed, most of the coherent $J/\psi$ events are classified correctly and the standard deviation of the $N_{J/\psi(coh)}$ is significantly smaller.

The $p_T$ fit to Monte Carlo data and its correlation matrix with the incoherent $J/\psi$ with proton dissociation contribution fixed can be seen in Fig. 3.7 and the number of events for the individual processes can be seen in Tab. 3.7.

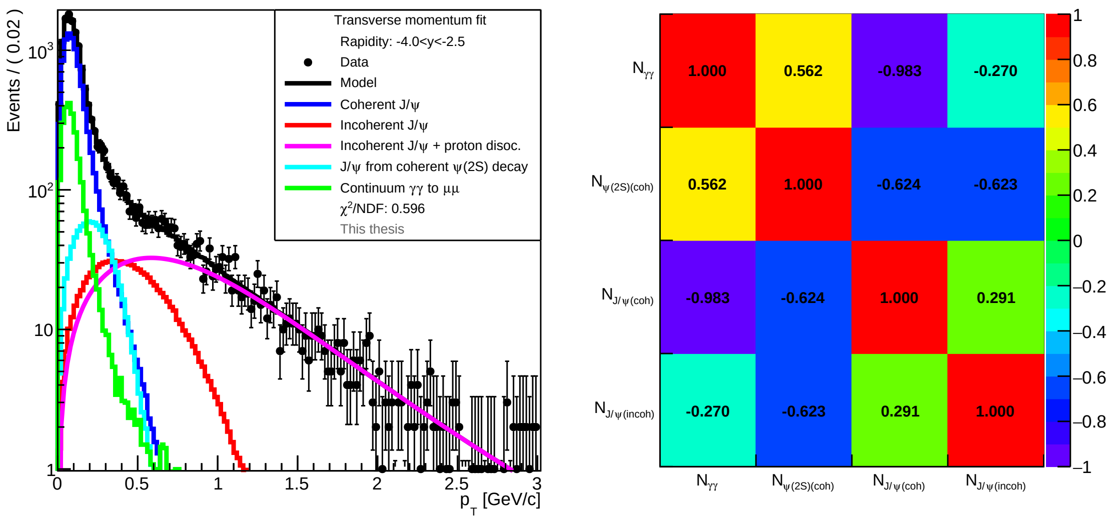


Figure 3.7: Fit to the transverse momentum spectrum of Monte Carlo data with a correlation matrix. The incoherent $J/\psi$ with proton dissociation contribution is fixed in the fit.

| **Process** | **#entries** | $N_{fit}$ | $\sqrt{N_{fit}}$ | $\sigma_{N_{fit}}$ |
|---|---|---|---|---|
| $N_{J/\psi(coh)}$ | 8241 | 8635 | 93 | 693 |
| $N_{J/\psi(incoh)}$ | 959 | 924 | 30 | 81 |
| $N_{\psi(2S)(coh)}$ | 781 | 872 | 30 | 127 |
| $N_{\gamma\gamma}$ | 2844 | 2408 | 49 | 634 |
| $N_{J/\psi(disoc)}$ | 1926 | 1926 | fixed | fixed |

Table 3.7: The number of events for given process, its square root (expected statistical uncertainty) and the standard deviation from the $p_T$ fit to Monte Carlo data with the incoherent $J/\psi$ with proton dissociation contribution fixed.

Fixing the incoherent $J/\psi$ with proton dissociation contribution does not bring any significant change to the fit results.

From the above results it is clear that fixing either the coherent J/$\psi$ contribution or the $\gamma\gamma$ background contribution significantly improves the fit. On the other hand fixing the other contributions does not meaningfully improve the fit.

The invariant mass fit can be used to be able to fix the $\gamma\gamma$ background contribution in real data. This procedure was first tested on Monte Carlo data, the invariant mass fit can be seen in Fig. 3.8.

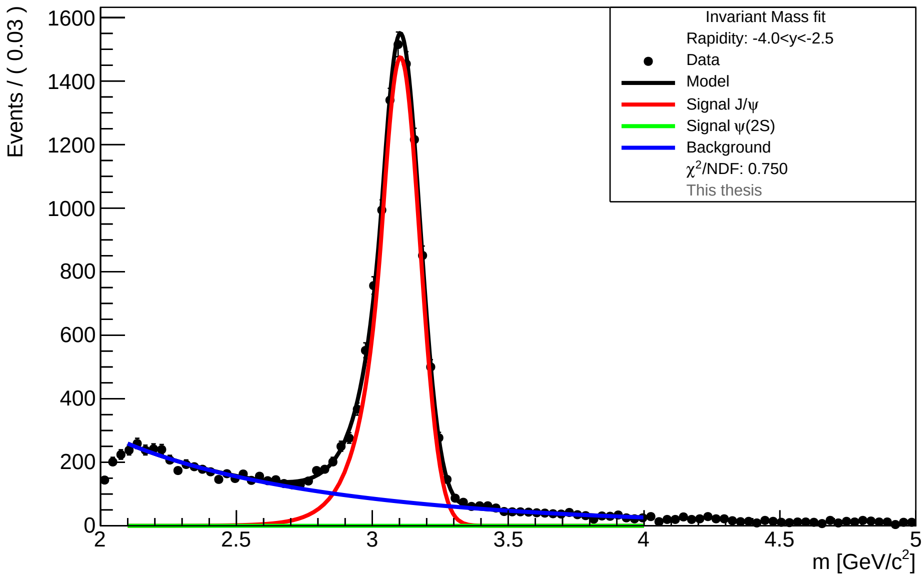


Figure 3.8: Fit to the invariant mass spectrum of Monte Carlo data.

The invariant mass fit gives for the background in the J/$\psi$ invariant mass windows $N_{\gamma\gamma}$ = 3010 $\pm$ 51. To constraint the $\gamma\gamma$ background in the $p_T$ distribution a -5% and +4% range from the $N_{\gamma\gamma}$ value was used. The $p_T$ fit to Monte Carlo data with this limitation and its correlation matrix can be seen in Fig. 3.9 and the number of events for the individual processes can be seen in Tab. 3.8.

The constrains helped to identify the correct number of coherent J/$\psi$ events as well as lower the standard deviation of the extracted number of events. However the fit did not find a stable solution for the number of $\gamma\gamma$ events within the parameter limits. The $N_{\gamma\gamma}$ = 2859 $\pm$ 258 is the value of the lower limit of the parameter.

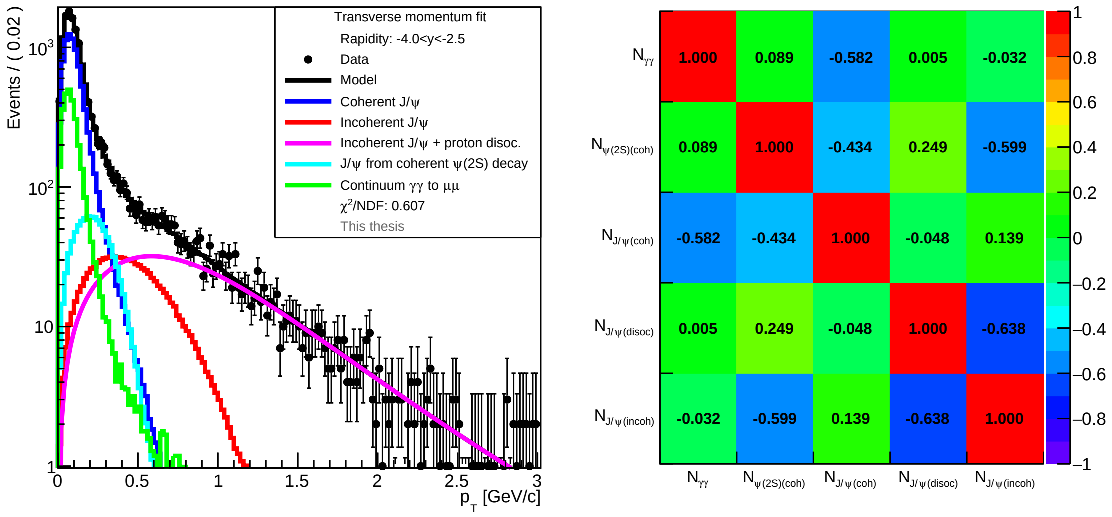


Figure 3.9: Fit to the transverse momentum spectrum of Monte Carlo data with a correlation matrix. The number of $\gamma\gamma$ events is constrained based on the invariant mass fit.

| **Process** | **#entries** | $N_{fit}$ | $\sqrt{N_{fit}}$ | $\sigma_{N_{fit}}$ |
|---|---|---|---|---|
| $N_{J/\psi(coh)}$ | 8241 | 8155 | 90 | 157 |
| $N_{J/\psi(incoh)}$ | 959 | 943 | 31 | 102 |
| $N_{\psi(2S)(coh)}$ | 781 | 908 | 30 | 109 |
| $N_{\gamma\gamma}$ | 2844 | 2859 | 53 | 258 |
| $N_{J/\psi(disoc)}$ | 1926 | 1887 | 43 | 71 |

Table 3.8: The number of events for given process, its square root (expected statistical uncertainty) and the standard deviation from the $p_T$ fit to Monte Carlo data. The number of $\gamma\gamma$ events is constrained based on the invariant mass fit.

The same procedure was repeated for real data. However, in the Monte Carlo invariant mass data sample there was no contribution from the incoherent J/$\psi$ production with proton dissociation, because Eq. 3.1 describes only the transverse momentum distribution. To account for this difference with respect to real data, the contribution from the incoherent J/$\psi$ production with proton dissociation was subtracted from the number of background events obtained from the invariant mass fit to real data which can be seen in Fig. 3.10.

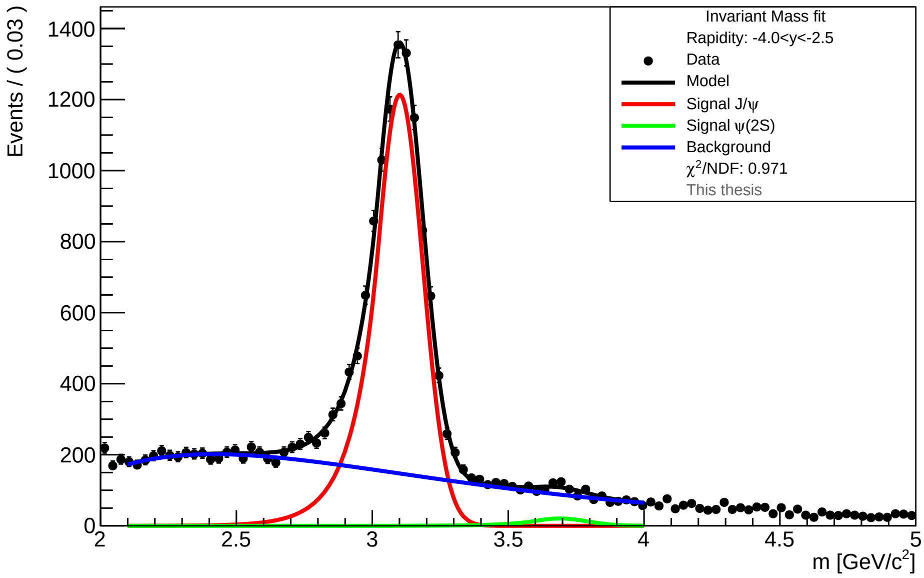


Figure 3.10: Fit to the invariant mass spectrum of real data.

The invariant mass fit gives for the background in the $J/\psi$ invariant mass windows $N_{\gamma\gamma}$ = 3279 $\pm$ 110. To constraint the $\gamma\gamma$ background in the $p_T$ distribution the -5% and +4% range from the $N_{\gamma\gamma}$ value was used again. In the invariant mass spectrum can be seen also the $\psi(2S)$ peak. The $\psi(2S)$ is not the object of this analysis, however it might be analysed in the future. The $p_T$ fit to real data with this limitation and its correlation matrix can be seen in Fig. 3.11 and the number of events for the individual processes can be seen in Tab. 3.9.

| **Process** | $N_{fit}$ | $\sqrt{N_{fit}}$ | $\sigma_{N_{fit}}$ |
|---|---|---|---|
| $N_{J/\psi(coh)}$ | 7918 | 89 | 175 |
| $N_{J/\psi(incoh)}$ | 945 | 31 | 102 |
| $N_{\psi(2S)(coh)}$ | 813 | 29 | 110 |
| $N_{\gamma\gamma}$ | 3115 | 56 | 294 |
| $N_{J/\psi(disoc)}$ | 1927 | 44 | 71 |

Table 3.9: The number of events for given process, its square root (expected statistical uncertainty) and the standard deviation from the $p_T$ fit to real data. The number of $\gamma\gamma$ events is constrained based on the invariant mass fit.

The procedure once again lowered the standard deviation of the number of extracted coherent $J/\psi$ and $\gamma\gamma$ background events. And again the fit took the value of the lower limit for the number of $\gamma\gamma$ events which is $N_{\gamma\gamma}$ = 3115 $\pm$ 294.

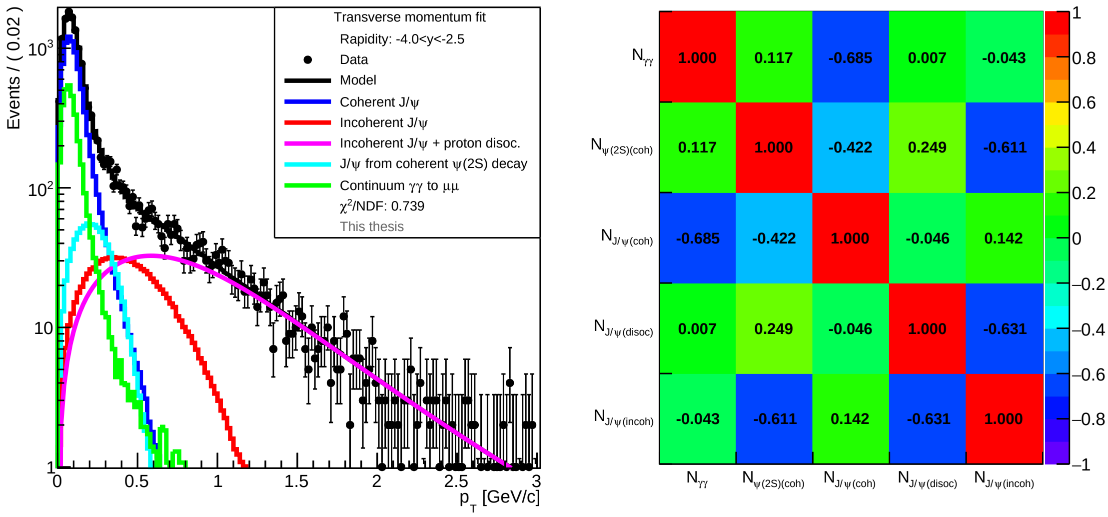


Figure 3.11: Fit to the transverse momentum spectrum of real data with a correlation matrix. The number of $\gamma\gamma$ events is constrained based on the invariant mass fit.

With the $N_{\gamma\gamma}$ parameter taking the lower limit value each time, this procedure has to be carefully tested to make sure of its validity. Dependence on bin width, fit range, sample size and other things have to be examined.

Another solution for constraining the number of $\gamma\gamma$ events is, instead of using one fit to limit the other, to do a simultaneous fit to both invariant mass and transverse momentum spectra. This technique will be tested in the future.

Once the coherent $J/\psi$ photoproduction yield is verified to be extracted correctly, the next step in the analysis to be able to compute the differential cross section from Eq. 2.3 is to determine the acceptance and efficiency correction factor, work on this step has just started.

# Summary

In the first chapter of this Research project are reviewed two theoretical papers on predictions for coherent $J/\psi$ photoproduction within the colour-dipole model in nucleus-nucleus and proton-nucleus ultra-peripheral collisions at RHIC and LHC.

In the second chapter are discussed two papers concerning the measurement of the coherent $J/\psi$ photoproduction in ultra-peripheral collisions by PHENIX at RHIC and by CMS at LHC. And also a paper by the ALICE collaboration which is the first paper reporting the coherent $J/\psi$ photoproduction measured in peripheral collisions.

The third chapter is devoted to the analysis of coherent $J/\psi$ photoproduction in ultra-peripheral Pb-Pb collisions at a centre-of-mass energy per nucleon $\sqrt{s_{NN}} = 5.02$ TeV measured with the ALICE detector in the forward rapidity region. The $J/\psi$ is reconstructed from its dimuon decay channel.

The main work was devoted to the extraction of the coherent contribution from the overall $J/\psi$ signal. This was done by fitting the transverse momentum spectrum with RooFit PDF templates based on STARLIGHT Monte Carlo simulations. However this method resulted in $\gamma\gamma$ background events being falsely identified as coherent $J/\psi$ events. Therefore a constraint on the number of $\gamma\gamma$ background events in the transverse momentum spectrum was applied. The constraint was obtained from a fit to the invariant mass spectrum. This method was successfully tested on Monte Carlo data and therefore was used for real data as well. However it will be further studied to make certain of its viability.

An alternative constraining method is to use a simultaneous fit instead of limiting one fit with another. This method will be implemented in the near future. Work on determining the acceptance times efficiency correction factor has started in order to be able to soon calculate the coherent $J/\psi$ photoproduction cross section.

# Bibliography


[1] T. Lappi and H. Mantysaari. $J/\psi$ production in ultraperipheral Pb+Pb and $p$+Pb collisions at energies available at the CERN Large Hadron Collider. *Phys. Rev.*, C87(3):032201, 2013.

[2] V. P. Goncalves and M. V. T. Machado. Vector Meson Production in Coherent Hadronic Interactions: An update on predictions for RHIC and LHC. *Phys. Rev.*, C84:011902, 2011.

[3] Tomáš Herman. Signal extraction in $J/\psi$ photoproduction in the alice experiment. Bachelor's thesis, Czech Technical University in Prague - Faculty of Nuclear Sciences and Physical Engineering, 2017.

[4] J. G. Contreras and J. D. Tapia Takaki. Ultra-peripheral heavy-ion collisions at the LHC. *Int. J. Mod. Phys.*, A30:1542012, 2015.

[5] E. Iancu, K. Itakura, and S. Munier. Saturation and BFKL dynamics in the HERA data at small x. *Phys. Lett.*, B590:199–208, 2004.

[6] G. Soyez. Saturation QCD predictions with heavy quarks at HERA. *Phys. Lett.*, B655:32–38, 2007.

[7] Henri Kowalski and Derek Teaney. An Impact parameter dipole saturation model. *Phys. Rev.*, D68:114005, 2003.

[8] H. Kowalski, L. Motyka, and G. Watt. Exclusive diffractive processes at HERA within the dipole picture. *Phys. Rev.*, D74:074016, 2006.

[9] Cyrille Marquet. A Unified description of diffractive deep inelastic scattering with saturation. *Phys. Rev.*, D76:094017, 2007.

[10] T. Lappi and H. Mantysaari. Incoherent diffractive $J/\psi$-production in high energy nuclear DIS. *Phys. Rev.*, C83:065202, 2011.

[11] E. Iancu, K. Itakura, and S. Munier. Saturation and BFKL dynamics in the HERA data at small x. *Phys. Lett.*, B590:199–208, 2004.

[12] Tobias Toll and Thomas Ullrich. Exclusive diffractive processes in electron-ion collisions. *Phys. Rev.*, C87(2):024913, 2013.

[13] Carlos A. Bertulani, Spencer R. Klein, and Joakim Nystrand. Physics of ultra-peripheral nuclear collisions. *Ann. Rev. Nucl. Part. Sci.*, 55:271–310, 2005.

[14] Betty Abelev et al. Coherent $J/\psi$ photoproduction in ultra-peripheral Pb-Pb collisions at $\sqrt{s_{NN}} = 2.76$ TeV. *Phys. Lett.*, B718:1273–1283, 2013.

[15] Christoph Mayer for the ALICE Collaboration. Cracow epiphany conference on the physics after the first phase of the LHC, 7–9.01.2013.
http://epiphany.ifj.edu.pl/epiphany.2013/pres/day2_Mayer_ALICE_Epiphany_v4.pdf.

[16] S. Afanasiev et al. Photoproduction of $J/\psi$ and of high mass $e^+e^-$ in ultra-peripheral Au+Au collisions at $\sqrt{s_{\mathrm{NN}}} = 200$ GeV. *Phys. Lett.*, B679:321–329, 2009.

[17] Gerhard Baur, Kai Hencken, Dirk Trautmann, Serguei Sadovsky, and Yuri Kharlov. Coherent $\gamma\gamma$ and $\gamma$A interactions in very peripheral collisions at relativistic ion colliders. *Physics Reports*, 364(5):359 – 450, 2002.
http://www.sciencedirect.com/science/article/pii/S0370157301001016.

[18] A. J. Baltz. The Physics of Ultraperipheral Collisions at the LHC. *Phys. Rept.*, 458:1–171, 2008.

[19] M. Drees and D. Zeppenfeld. Production of supersymmetric particles in elastic ep collisions. *Phys. Rev. D*, 39:2536–2546, May 1989.
https://link.aps.org/doi/10.1103/PhysRevD.39.2536.

[20] N.N. Nikolaev and B.G. Zakharov. On determination of the large-1x gluon distribution at hera. *Physics Letters B*, 332(1):184 – 190, 1994.
http://www.sciencedirect.com/science/article/pii/037026939490877X.

[21] V. P. Gonçalves and M. V. T. Machado. Nuclear exclusive vector meson photoproduction. *The European Physical Journal C - Particles and Fields*, 38(3):319–328, Dec 2004.
https://doi.org/10.1140/epjc/s2004-02044-7.

[22] J. Bartels, Krzysztof J. Golec-Biernat, and Krisztian Peters. On the dipole picture in the nonforward direction. *Acta Phys. Polon.*, B34:3051–3068, 2003.

[23] N. Armesto. A simple model for nuclear structure functions at small $x$ in the dipole picture. *Eur. Phys. J. C*, 26(1):35–43, 2002.
https://doi.org/10.1007/s10052-002-1021-z.

[24] C. Marquet, R. Peschanski, and G. Soyez. Exclusive vector meson production at hera from qcd with saturation. *Phys. Rev. D*, 76:034011, Aug 2007.
https://link.aps.org/doi/10.1103/PhysRevD.76.034011.

[25] Anthony J. Baltz, Spencer R. Klein, and Joakim Nystrand. Coherent vector-meson photoproduction with nuclear breakup in relativistic heavy-ion collisions. *Phys. Rev. Lett.*, 89:012301, Jun 2002.
https://link.aps.org/doi/10.1103/PhysRevLett.89.012301.

[26] Vardan Khachatryan et al. Coherent $J/\psi$ photoproduction in ultra-peripheral PbPb collisions at $\sqrt{s_{\mathrm{NN}}} = 2.76$ TeV with the CMS experiment. *Phys. Lett.*, B772:489–511, 2017.

[27] Jaroslav Adam et al. Measurement of an excess in the yield of $J/\psi$ at very low $p_{\mathrm{T}}$ in Pb-Pb collisions at $\sqrt{s_{\mathrm{NN}}}$ = 2.76 TeV. *Phys. Rev. Lett.*, 116(22):222301, 2016.

[28] C. Alexa et al. Elastic and Proton-Dissociative Photoproduction of $J/\psi$ Mesons at HERA. *Eur. Phys. J.*, C73(6):2466, 2013.

[29] John Erthal Gaiser. *Charmonium Spectroscopy From Radiative Decays of the* $J/\psi$ *and* $\psi'$. PhD thesis, SLAC, 1982.
http://www-public.slac.stanford.edu/sciDoc/docMeta.aspx?slacPubNumber=slac-r-255.html.

[30] E. Kryshen K. Graham, O.V. Baillie. Forward $J/\psi$ photoproduction in ultra-peripheral Pb-Pb collisions at $\sqrt{s_{NN}} = 5.02$ TeV. February 2017. Draft of an ALICE analysis note.